

GLOBAL PROPERTIES OF X-RAY FLASHES AND X-RAY-RICH GAMMA-RAY BURSTS OBSERVED BY *SWIFT*

T. SAKAMOTO,^{1,2} D. HULLINGER,³ G. SATO,^{1,4} R. YAMAZAKI,⁵ L. BARBIER,¹ S. D. BARTHELMEY,¹ J. R. CUMMINGS,^{1,6}
E. E. FENIMORE,⁷ N. GEHRELS,¹ H. A. KRIMM,^{1,8} D. Q. LAMB,⁹ C. B. MARKWARDT,^{1,10} J. P. OSBORNE,¹¹
D. M. PALMER,⁷ A. M. PARSONS,¹ M. STAMATIKOS,^{1,2} AND J. TUELLER¹

Received 2007 July 14; accepted 2008 January 27

ABSTRACT

We describe and discuss the spectral and temporal characteristics of the prompt emission and X-ray afterglow emission of X-ray flashes (XRFs) and X-ray-rich gamma-ray bursts (XRRs) detected and observed by *Swift* between 2004 December and 2006 September. We compare these characteristics to a sample of conventional classical gamma-ray bursts (C-GRBs) observed during the same period. We confirm the correlation between $E_{\text{peak}}^{\text{obs}}$ and fluence noted by others and find further evidence that XRFs, XRRs, and C-GRBs form a continuum. We also confirm that our known redshift sample is consistent with the correlation between the peak energy in the GRB rest frame ($E_{\text{peak}}^{\text{src}}$) and the isotropic radiated energy (E_{iso}), the so-called $E_{\text{peak}}^{\text{src}}-E_{\text{iso}}$ relation. The spectral properties of X-ray afterglows of XRFs and C-GRBs are similar, but the temporal properties of XRFs and C-GRBs are quite different. We found that the light curves of C-GRB afterglows show a break to steeper indices (shallow-to-steep break) at much earlier times than do XRF afterglows. Moreover, the overall luminosity of XRF X-ray afterglows is systematically smaller by a factor of 2 or more compared to that of C-GRBs. These distinct differences between the X-ray afterglows of XRFs and C-GRBs may be the key to understanding not only the mysterious shallow-to-steep break in X-ray afterglow light curves, but also the unique nature of XRFs.

Subject headings: gamma rays: bursts — X-rays: bursts

Online material: color figures

1. INTRODUCTION

Despite the rich gamma-ray burst (GRB) sample provided by BATSE (e.g., Paciesas et al. 1999; Kaneko et al. 2006), *BeppoSAX* (e.g., Frontera 2004), *Konus-Wind* (e.g., Ulanov et al. 2005), and *HETE-2* (e.g., Barraud et al. 2003; Sakamoto et al. 2005), the emission properties of GRBs are still far from being well understood. In recent years, however, another phenomenon that resembles GRBs in almost every way, except that the flux comes mostly from X-rays instead of γ -rays, has been discovered and studied. This new class of bursts has been dubbed “X-ray flashes” (XRFs; Heise et al. 2003; Barraud et al. 2003; Sakamoto et al. 2005), and there is strong evidence to suggest that “classical” GRBs (C-GRBs) and XRFs are closely related phenomena. Understanding what physical processes lead to their differences could yield important insights into their nature and origin.

Strohmayer et al. (1998) identified 22 bursts observed by *Ginga* that occurred between 1987 March and 1991 October and for which the spectra could be reliably analyzed. About 36% of GRBs observed by *Ginga* had very soft spectra. They noted that these bursts resembled BATSE long GRBs in duration and general spectral shape, but the peak energies of the νF_{ν} spectrum, $E_{\text{peak}}^{\text{obs}}$, extended to lower values than those of the BATSE bursts (Preece et al. 2000; Kaneko et al. 2006). Heise et al. (2003) reported that among the sources imaged by the Wide Field Cameras (WFCs) on board *BeppoSAX* was a class of fast X-ray transients with durations of less than 1000 s that were not “triggered” (i.e., detected) by the Gamma Ray Burst Monitor (GRBM). This became their working definition of XRFs. Kippen et al. (2003) searched for C-GRBs and XRFs, which were observed simultaneously by WFC and BATSE. They found 36 C-GRBs and 17 XRFs in a 3.8 year period. Joint WFC and BATSE spectral analysis was performed for the sample, and they found that XRFs have a significantly lower $E_{\text{peak}}^{\text{obs}}$ compared with C-GRBs. They also found that there is no systematic difference between XRFs and C-GRBs in their low-energy photon indices, high-energy photon indices, or durations. The systematic spectral analysis of a sample of 45 *HETE-2* GRBs confirmed these spectral and temporal characteristics of XRFs. It is worth noting that nine out of 16 XRF samples of *HETE-2* have $E_{\text{peak}}^{\text{obs}} < 20$ keV (Barraud et al. 2003; Sakamoto et al. 2005).

Although the XRF prompt emission properties have been studied, until the launch of *Swift* (Gehrels et al. 2004), only a handful of X-ray afterglows associated with XRFs were reported. D’Alessio et al. (2006) studied the prompt and afterglow emission of XRFs and X-ray-rich GRBs (XRRs) observed by *BeppoSAX* and *HETE-2*. They found that the XRF and XRR afterglow light curves seem to be similar to those of C-GRBs, including the break feature in the light curves. They also investigated the off-axis viewing scenarios of XRFs

¹ NASA Goddard Space Flight Center, Greenbelt, MD 20771.

² Oak Ridge Associated Universities, P.O. Box 117, Oak Ridge, TN 37831-0117.

³ Moxtek, Inc., 452 West 1260 North, Orem, UT 84057.

⁴ Institute of Space and Astronautical Science, JAXA, Kanagawa 229-8510, Japan.

⁵ Department of Physics, Hiroshima University, Higashi-Hiroshima 739-8526, Japan.

⁶ Joint Center for Astrophysics, University of Maryland, Baltimore County, 1000 Hilltop Circle, Baltimore, MD 21250.

⁷ Los Alamos National Laboratory, P.O. Box 1663, Los Alamos, NM 87545.

⁸ Universities Space Research Association, 10211 Wincopin Circle, Suite 500, Columbia, MD 21044-3432.

⁹ Department of Astronomy and Astrophysics, University of Chicago, Chicago, IL 60637.

¹⁰ Department of Physics, University of Maryland, College Park, MD 20742.

¹¹ Department of Physics and Astronomy, University of Leicester, LE1, 7RH, UK.

for the top-hat-shaped jet (Yamazaki et al. 2002, 2004), the universal power-law-shaped jet (Rossi et al. 2002; Zhang & Mészáros 2002; Lamb et al. 2005), and the Gaussian jet (Zhang et al. 2004), and they concluded that these models might be consistent with the data. Their sample, however, only contains nine XRFs/XRRs with measured X-ray afterglows. Furthermore, the data points in the X-ray light curves were not well sampled, so that there are large uncertainties in the decay indices and the overall structures of the light curve in most cases. Moreover, since the X-ray afterglow observations began $>10^4$ s after the trigger, their sample is able to say little about the early afterglow properties, which contain rich information that can constrain jet models for XRFs. Other XRF theoretical models are the inhomogeneous jet model (Toma et al. 2005), the internal shock emission from high bulk Lorentz factor shells (Mochkovitch et al. 2003; Barraud et al. 2005), the external shock emission from low bulk Lorentz factor shells (Dermer et al. 1999; Dermer & Mitman 2003), and the X-ray emission from the hot cocoon of the GRB jet if viewed from off-axis (Mészáros et al. 2002; Woosley et al. 2003).

Because of the sophisticated on-board localization capability of the *Swift* Burst Alert Telescope (BAT; Barthelmy et al. 2005) and the fast spacecraft pointing of *Swift*, more than 90% of *Swift* GRBs have an X-ray afterglow observation from the *Swift* X-Ray Telescope (XRT; Burrows et al. 2005a) within a few hundred seconds after the trigger. Due to the fact that BAT is sensitive to relatively low energies (15–150 keV) and also a large effective area (~ 1000 cm² at 20 keV for a source on-axis), BAT is also detecting XRFs and XRRs. However, because of BAT's lack of response below 15 keV, it is very challenging to detect XRFs with $E_{\text{peak}}^{\text{obs}}$ of a few keV, which dominated the XRF samples of *BeppoSAX* and *HETE-2* (e.g., Kippen et al. 2003; Sakamoto et al. 2005). Nonetheless, *Swift* has a unique capability for studying detailed X-ray afterglow properties just after the burst for XRFs and XRRs with $E_{\text{peak}}^{\text{obs}} \gtrsim 20$ keV for the first time.

The systematic study of the X-ray emissions of GRBs observed by XRT reveals a very complex power-law decay behavior consisting typically of an initial very steep decay (t^α with $-10 \lesssim \alpha_1 \lesssim -2$) (e.g., O'Brien et al. 2006; Sakamoto et al. 2007), followed by a shallow decay ($-1 \lesssim \alpha_2 \lesssim 0$), followed by a steeper decay ($-2 \lesssim \alpha_3 \lesssim -1$; e.g., Nousek et al. 2006; O'Brien et al. 2006; Willingale et al. 2007), sometimes followed by a much steeper decay ($\alpha_4 \lesssim -2$; e.g., Willingale et al. 2007) and, in some cases (about 50%), overlaid X-ray flares (e.g., Burrows et al. 2005b; Chincarini et al. 2007; Kocevski et al. 2007). Although there is increasing evidence that the initial very steep decay component α_1 is a tail of the GRB prompt emission (e.g., Liang et al. 2006; Sakamoto et al. 2007), the origin of the phase from a shallow α_2 to a steeper decay α_3 (hereafter a shallow-to-steep decay) is still a mystery. Moreover, not all GRBs have a shallow-to-steep decay phase in their X-ray afterglow light curves. Thus, it is very important to investigate the X-ray afterglow light curves of bursts along with their prompt emission properties to find a difference in their characteristics between C-GRBs and XRFs.

In this paper, we report the systematic study of the prompt and afterglow emission of 10 XRFs and 17 XRRs observed by *Swift* from 2004 December through 2006 September. Although the data from *Swift* BAT are the primary data set for investigation of the prompt emission properties, we also use information from *Konus-Wind* and *HETE-2* as reported on the Gamma-ray burst Coordinate Network¹² or in the literature, when available, to

obtain better constraints on $E_{\text{peak}}^{\text{obs}}$. We focus on X-ray afterglow properties observed by the *Swift* XRT in this study. In § 2, we discuss our classification of GRBs, the analysis methods of the BAT and the XRT data, and the selection criteria of our sample. In §§ 3 and 4, we show the results of the prompt emission and the X-ray afterglow analysis, respectively. We found distinct differences between XRFs and C-GRBs in the shape and in the overall luminosity of X-ray afterglows. We discuss the implications of our results in § 5. Our conclusions are summarized in § 6. We used the cosmological parameters of $\Omega_m = 0.3$, $\Omega_\Lambda = 0.7$, and $H_0 = 70$ km s⁻¹ Mpc⁻¹. The quoted errors are at the 90% confidence level unless stated otherwise.

2. ANALYSIS

2.1. Working Definition of Swift GRBs and XRFs

The precise working definitions adopted by others who have studied XRFs have tended (understandably) to be based on the characteristics and energy sensitivities of the instruments that collected the data (Gotthelf et al. 1996; Strohmayer et al. 1998; Heise et al. 2003; Sakamoto et al. 2005). The effective area of the BAT is sufficiently different from these other instruments that none of the definitions previously adopted are quite suitable (Band 2003, 2006). We desire a definition, however, that will correspond to previous definitions so that we may reliably compare the characteristics of the BAT-detected XRF population with those from other missions. Sakamoto et al. (2005) defined XRFs in terms of the fluence ratio $S_X(2\text{--}30 \text{ keV})/S_\gamma(30\text{--}400 \text{ keV})$, and C-GRBs, XRRs, and XRFs were classified according to this fluence ratio. Sakamoto et al. (2005) noted a strong correlation between the observed spectral peak energy $E_{\text{peak}}^{\text{obs}}$ and the fluence ratio. They found that the border $E_{\text{peak}}^{\text{obs}}$ between XRFs and XRRs is ≈ 30 keV, and the border $E_{\text{peak}}^{\text{obs}}$ between XRRs and C-GRBs is ≈ 100 keV.

In the BAT energy range, a fluence ratio of $S(25\text{--}50 \text{ keV})/S(50\text{--}100 \text{ keV})$ is more natural and easier to measure with confidence. We therefore chose our working definition in terms of this ratio. In order to ensure that our definition is close to that adopted by Sakamoto et al. (2005) we calculated the fluence ratio of a burst for which the parameters of the Band function¹³ (Band et al. 1993) are $\Gamma_1 = -1$, $\Gamma_2 = -2.5$, and $E_{\text{peak}}^{\text{obs}} = 30$ keV. These values of Γ_1 and of Γ_2 are typical of the distributions for XRFs, XRRs, and C-GRBs found by BATSE (Preece et al. 2000; Kaneko et al. 2006), *BeppoSAX* (Kippen et al. 2003), and *HETE-2* (Sakamoto et al. 2005). The ratio thus found is 1.32. We likewise calculated the fluence ratio of a burst for which $\Gamma_1 = -1$, $\Gamma_2 = -2.5$, and $E_{\text{peak}}^{\text{obs}} = 100$ keV, which was found to be 0.72. Our working definition of XRFs, XRRs, and C-GRBs thus becomes

$$\begin{aligned} S(25\text{--}50 \text{ keV})/S(50\text{--}100 \text{ keV}) &\leq 0.72 \quad (\text{C-GRB}), \\ 0.72 < S(25\text{--}50 \text{ keV})/S(50\text{--}100 \text{ keV}) &\leq 1.32 \quad (\text{XRR}), \\ S(25\text{--}50 \text{ keV})/S(50\text{--}100 \text{ keV}) &> 1.32 \quad (\text{XRF}). \end{aligned} \quad (1)$$

To check the consistency of our definition, we calculated $S(25\text{--}50 \text{ keV})$ and $S(50\text{--}100 \text{ keV})$ of the *HETE-2* sample using the best-fit time-averaged spectral parameters reported in Sakamoto et al. (2005). The 90% error in the fluences is calculated by scaling the associated error in the normalization of the best-fit spectral model. As shown in Figure 1, our definition is consistent with the *HETE-2* definition of XRFs, XRRs, and C-GRBs (Sakamoto et al. 2005).

¹³ $f(E) = K_1 E^{\Gamma_1} \exp[-E(2 + \Gamma_1)/E_{\text{peak}}]$ if $E < (\Gamma_1 - \Gamma_2)E_{\text{peak}}/(2 + \Gamma_1)$ and $f(E) = K_2 E^{\Gamma_2}$ if $E \geq (\Gamma_1 - \Gamma_2)E_{\text{peak}}/(2 + \Gamma_1)$.

¹² See http://gcn.gsfc.nasa.gov/gcn_main.html.

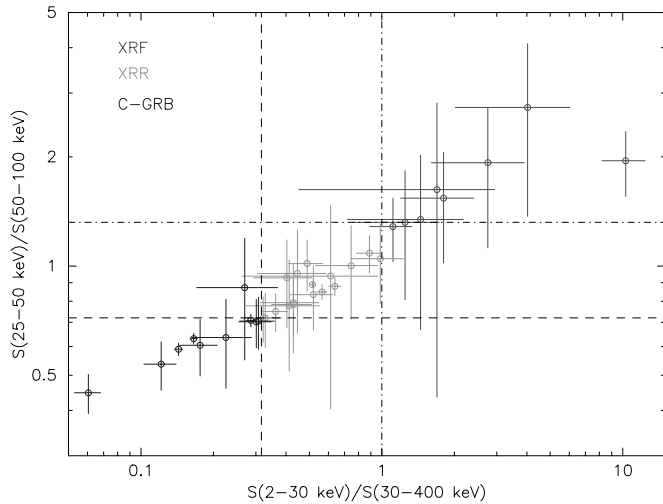


FIG. 1.— $S(2-30 \text{ keV})/S(30-400 \text{ keV})$ and $S(25-50 \text{ keV})/S(50-100 \text{ keV})$ fluence ratios of *HETE-2* bursts. The dashed and dash-dotted lines correspond to the borders between C-GRBs and XRRs, and between XRRs and XRFs, respectively. [See the electronic edition of the *Journal* for a color version of this figure.]

2.2. *Swift* BAT Data Analysis

All the event data from *Swift* BAT are available through HEASARC at NASA Goddard Space Flight Center. We used the standard BAT software (HEADAS 6.1.1) and the latest calibration database (CALDB: 2006-05-30). The burst pipeline script, `batgrbproduct`, was used to process the BAT event data. The `xspec` spectral fitting tool (ver. 11.3.2) was used to fit each spectrum.

For the time-averaged spectral analysis, we use the time interval from 0% to 100% of the total burst fluence (t_{100} interval) calculated by `batblocks`. Since the BAT energy response generator, `batdrngen`, performs the calculation for a fixed single incident angle of the source, it will be a problem if the position of the source is moving during the time interval selected for the spectral analysis due to the spacecraft slew. In this situation, we created the response matrices for each 5 s period during the time interval taking into account the position of the GRB in detector coordinates. We then weighted these response matrices by the 5 s count rates and created the averaged response matrices using `addrmf`. Since the spacecraft slews about 1° per second in response to a GRB trigger, we chose 5 s intervals to calculate the energy response for every 5° .

We fit each spectrum with a power-law (PL) model¹⁴ and a cutoff power-law (CPL) model.¹⁵ The best-fit spectral model is determined based on the difference in χ^2 between a PL and a CPL fit. If $\Delta\chi^2$ between a PL and a CPL fit is greater than 6 ($\Delta\chi^2 \equiv \chi_{\text{PL}}^2 - \chi_{\text{CPL}}^2 > 6$), we determine that a CPL model is a better representative spectral model for the data. To quantify the significance of this improvement, we performed 10,000 spectral simulations taking into account the distributions of the power-law photon index in a PL fit, the fluence in the 15–150 keV band in a PL fit, and the t_{100} duration of the BAT GRBs (e.g., Sakamoto et al. 2008), and we determined in how many cases a CPL fit gives χ^2 improvements of ≥ 6 over a PL fit. We used the best-fit normal distribution for the power-law photon index centering on 1.65 with σ of 0.36. The best-fit lognormal distribution is used for the fluence centering on $S(15-150 \text{ keV}) = 10^{-5.92} \text{ ergs cm}^{-2}$

¹⁴ $f(E) = K_{50}(E/50 \text{ keV})^\Gamma$, where K_{50} is the normalization at 50 keV in units of photons $\text{cm}^{-2} \text{ s}^{-1} \text{ keV}^{-1}$.

¹⁵ $f(E) = K_{50}(E/50 \text{ keV})^\Gamma \exp[-E(2 + \Gamma)/E_{\text{peak}}]$.

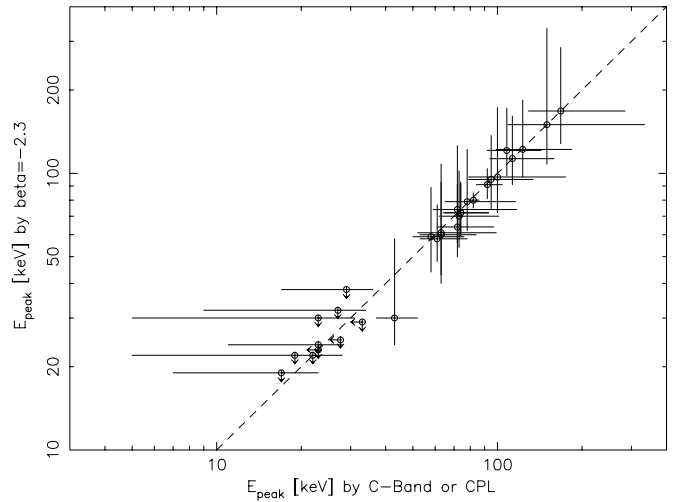


FIG. 2.—Relationship between $E_{\text{peak}}^{\text{obs}}$ derived by the Band function with a fixed high-energy photon index $\Gamma_2 = -2.3$ and $E_{\text{peak}}^{\text{obs}}$ derived by the C-Band function or a CPL model.

with σ of $S(15-150 \text{ keV}) = 10^{0.59} \text{ ergs cm}^{-2}$. In addition, the best-fit lognormal distribution is used for the t_{100} duration centering on $t_{100} = 10^{1.74} \text{ s}$ with a σ of $t_{100} = 10^{0.53} \text{ s}$. The BAT energy response matrix used in the simulation corresponds to an incident angle of 30° , which is the average of the BAT GRB samples. We found equal or higher improvements in χ^2 in 62 simulated spectra out of 10,000. Thus, the chance probability of having an equal or higher $\Delta\chi^2$ of 6 with a CPL model when the parent distribution is a case of a PL model is 0.62%.

Because of the narrow energy band of the BAT, most of the $E_{\text{peak}}^{\text{obs}}$ values measured from the BAT spectral data are based on a CPL fit, but not on the Band function fit. For XRFs, we apply a *constrained* Band (hereafter C-Band) function method (Sakamoto et al. 2004) to constrain $E_{\text{peak}}^{\text{obs}}$. However, there is a systematic problem in the $E_{\text{peak}}^{\text{obs}}$ values derived by different spectral models. In particular, for the bursts for which the true spectral shape is the Band function, there is a known effect that $E_{\text{peak}}^{\text{obs}}$ derived from a CPL model fit has a systematically higher value than $E_{\text{peak}}^{\text{obs}}$ derived from a Band function fit (e.g., Kaneko et al. 2006; Cabrera et al. 2007). To investigate this effect, we fit all the BAT GRB spectra for which $E_{\text{peak}}^{\text{obs}}$ are derived only from the BAT data with a Band function with the high-energy photon index fixed at Γ_2 to -2.3 . Figure 2 shows $E_{\text{peak}}^{\text{obs}}$ derived by the Band function fixing $\Gamma_2 = -2.3$ and $E_{\text{peak}}^{\text{obs}}$ derived by a CPL or a C-Band function. The $E_{\text{peak}}^{\text{obs}}$ values derived by the Band function with fixing $\Gamma_2 = -2.3$ and by a CPL model agree within errors. Most of $E_{\text{peak}}^{\text{obs}}$ values derived by a C-Band function also agree with $E_{\text{peak}}^{\text{obs}}$ derived by the Band function with fixing $\Gamma_2 = -2.3$ to within errors. Therefore, we conclude that the systematic error in $E_{\text{peak}}^{\text{obs}}$ derived by different spectral models is negligible compared to that of the statistical error assigned to $E_{\text{peak}}^{\text{obs}}$ derived from the BAT spectral data alone. Note that the BAT spectral data include the systematic errors, which are introduced to reproduce the canonical spectrum of the Crab nebula observed at various incident angles (Sakamoto et al. 2008). To perform the systematic study using the BAT data, we only selected bursts for which the full BAT event data are available.¹⁶

¹⁶ We exclude bursts such as GRB 050820A, GRB 051008, and GRB 060218 because of incomplete event data.

2.3. *Swift* XRT Data

We constructed a pipeline script to perform the XRT analysis in a systematic way. This pipeline script analysis is composed of four parts: (1) data download from the *Swift* Science Data Center (SDC); (2) an image analysis to find the source (X-ray afterglow) and background regions; (3) a temporal analysis to construct and fit the light curve; and (4) a spectral analysis. The screened event data of the Window Timing (WT) mode and the Photon Counting (PC) mode are downloaded from the SDC and used in our pipeline process. For the WT mode, only the data of the first segment number (001) are selected. All available PC mode data are applied. The standard grades, grades 0–2 for the WT mode and 0–12 for the PC mode, are used in the analysis. The analysis is performed in the 0.3–10 keV band. The detection of an X-ray afterglow is done automatically using `ximage` assuming that an afterglow is the brightest X-ray source located within $4'$ from the BAT on-board position. However, in cases where a steady cataloged bright X-ray source is misidentified as an afterglow, we specify the coordinates of the X-ray afterglow manually. The source region of the PC mode is selected as a circle of $47''$ radius. The background region of the PC mode is an annulus in an outer radius of $150''$ and an inner radius of $70''$ excluding the background X-ray sources detected by `ximage` in circular regions of $47''$ radius. For the WT data, the rectangular region of $1.6' \times 6.7'$ is selected as a foreground region using an afterglow position derived from the PC mode data as the center of the region. The background region is selected to be a square region of $6.7'$ on a side excluding a $2.3' \times 6.7'$ rectangular region centered at the afterglow position. The light curve is binned based on the number of photons required to meet at least 5σ for the PC mode and 10σ for the WT mode in each light curve bin. The light curve fitting starts with a single power law. Then, additional power-law components are added to minimize χ^2 of the fit. Complicated structures such as X-ray flares are also well fitted with this algorithm. Although our pipeline script fits the XRT light curve automatically for every GRB trigger by this algorithm, we excluded the time intervals during the X-ray flares from the light curve data by visual inspections before doing the fit by our method because the understanding of the overall shape of the light curve is the primary interest in our study. The ancillary response function (ARF) files are created by `xrtmkarf` for the WT and the PC mode data individually. The spectral fitting is performed by `xspec 11.3.2` using an absorbed power-law model¹⁷ for both the WT and the PC mode data. For an absorption model, we fix the Galactic absorption of Dickey & Lockman (1990) at the GRB location and then add an additional absorption to the model. We use the `xspec zwabs` model for known redshift GRBs applying the measured redshift to calculate the absorption associated to the source frame of GRBs. The spectra are binned to at least 20 counts in each spectral bin by `grppha`. The conversion factor from a count rate to an unabsorbed 0.3–10 keV energy flux is also calculated based on the result of the time-integrated spectral analysis.

A “pile-up” correction (e.g., Romano et al. 2006; Nousek et al. 2006; Evans et al. 2007) is applied during our pipeline process. It assumes a “pile-up” effect exists whenever the uncorrected count rate in the processed light curve exceeds 0.6 and 100 counts s^{-1} for the PC and the WT modes, respectively. Only the time intervals that are affected by the “pile-up” as described in our definition above have corrections applied. Although the area of the spectral region affected by pile-up depends on its

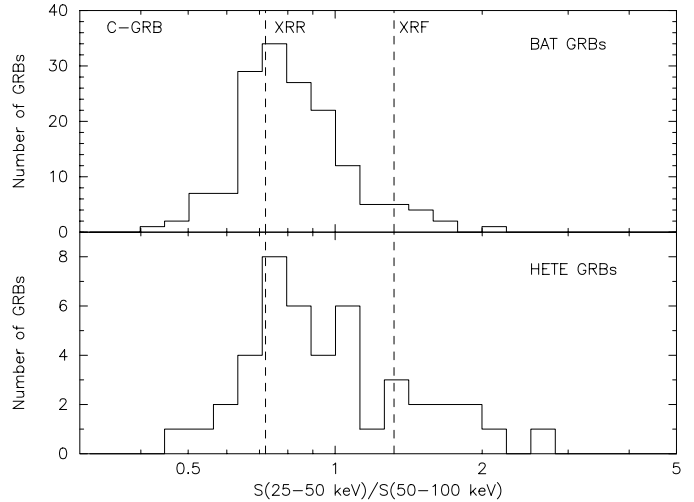


FIG. 3.—Distributions of the fluence ratio $S(25-50 \text{ keV})/S(50-100 \text{ keV})$ for BAT (top) and HETE-2 (bottom). The dashed lines correspond to the borders between C-GRBs and XRRs, and between XRRs and XRFs.

count rate, the script always eliminates a central area within $7''$ radius for the PC data and a $14'' \times 6.7'$ box region for the WT data. The count rate derived from the region excluding the central part is corrected by taking into account the shape of the ARF at an averaged photon energy. The spectral analysis is performed using only the data of $<0.6 \text{ counts s}^{-1}$ for the PC mode and $<100 \text{ counts s}^{-1}$ for the WT mode.

Two GRBs in our sample, GRB 050713A and GRB 060206 have a background X-ray source $\sim 25''$ and $\sim 10''$, respectively, from the position of the afterglow. Since it is difficult to exclude the contamination from the very closely located background source, we excluded the last portion of the light curves, which have a flattening that is very likely due to the contamination from the background source.

2.4. Sample of GRBs

We calculated the fluence ratio between the 25–50 keV and the 50–100 keV bands derived from a PL model using the BAT time-averaged spectrum for all *Swift* bursts detected between 2004 December and 2006 September. Then we classified these GRBs using the definition described in § 2.1. Out of a total of 158 long GRBs, we classified 10 as XRFs, 97 as XRRs, and 51 as C-GRBs. The distribution of the fluence ratio $S(25-50 \text{ keV})/S(50-100 \text{ keV})$ for the 158 long GRBs is shown in Figure 3. Similar to the HETE-2 results (Sakamoto et al. 2005), the figure clearly shows that *Swift*’s XRFs, XRRs, and C-GRBs also form a single broad distribution. This figure also clearly shows that the ratio of the number of BAT XRFs to BAT XRRs is smaller than that of the HETE-2 XRF samples. As discussed in Band (2006) the numbers of each GRB class strongly depend on the sensitivity of the instrument. This problem becomes more serious for the instruments that do not cover a wide energy range, such as the BAT. Thus, we will not discuss the absolute numbers of each GRB class in this paper.

Since the determination of $E_{\text{peak}}^{\text{obs}}$ is crucial for our study, we only select GRBs having values for $E_{\text{peak}}^{\text{obs}}$ that can be determined from the BAT data alone or from using the data from other GRB instruments (*Konus-Wind* and HETE-2). Since we can use the C-Band function method for XRFs to constrain $E_{\text{peak}}^{\text{obs}}$ if the photon index Γ in a PL fit is much steeper than -2 in the BAT spectrum, we select all bursts that have $\Gamma < -2$ at a 90% confidence level. We exclude GRB 041224 from our sample because there is no XRT observation. We also exclude GRB 060614 because there was no report on the time-averaged spectral

¹⁷ The `wabs * wabs * pegpwrhw` or `wabs * zwabs * pegpwrhw` model in `xspec`.

TABLE 1
PROMPT EMISSION PROPERTIES OF 41 *Swift* BURSTS

GRB	PL				CPL				OTHER		
	T_{100}^{BATa}	Γ	K_{50}^{d}	χ^2_{e}	$E_{\text{peak}}^{\text{obs}}$ (keV)	K_{50}^{g} (10^{-3} photons $\text{cm}^{-2} \text{s}^{-1} \text{keV}^{-1}$)	χ^2_{e}	$E_{\text{peak}}^{\text{f}}$	Mo/Inst ^h	$S(15-150 \text{ keV})^{\text{b}}$	SR23 ^c
XRF 050406	6.4	$-2.4^{+0.3}_{-0.3}$	13 ± 4	82.7	29^{+7}_{-12}	C-Band	0.79 ± 0.17	1.3 ± 0.6
XRF 050416A	3.0	-3.1 ± 0.2	98 ± 17	58.8	17^{+6}_{-10}	C-Band	3.7 ± 0.4	2.1 ± 0.6
XRF 050714B	50.3	-2.4 ± 0.3	12 ± 3	45.3	27^{+7}_{-18}	C-Band	6.0 ± 1.1	1.4 ± 0.5
XRF 050819	47.3	-2.7 ± 0.3	7 ± 2	57.1	22^{+6}_{-17}	C-Band	3.5 ± 0.5	1.6 ± 0.6
XRF 050824	26.6	-2.8 ± 0.4	9 ± 3	49.9	<19	C-Band	2.7 ± 0.5	1.6 ± 0.8
XRF 060219	65.3	$-2.6^{+0.3}_{-0.4}$	6 ± 2	59.6	<33	C-Band	4.3 ± 0.8	1.4 ± 0.6
XRF 060428B	65.7	-2.6 ± 0.2	12 ± 2	66.7	23^{+5}_{-12}	19^{+210}_{-15}	59.1	8.2 ± 0.8	1.5 ± 0.3
XRF 060512	9.7	-2.5 ± 0.3	24 ± 5	36.1	23^{+8}_{-18}	C-Band	2.3 ± 0.4	1.4 ± 0.5
XRF 060923B	9.9	$-2.5^{+0.2}_{-0.3}$	49 ± 8	56.9	<27.6	C-Band	4.8 ± 0.6	1.4 ± 0.4
XRF 060926	8.7	-2.5 ± 0.2	25 ± 4	58.5	<23	C-Band	2.2 ± 0.3	1.5 ± 0.4
XRR 050219B	76.1	-1.54 ± 0.05	224 ± 7	86.6	108^{+35}_{-8}	39^{+10}_{-8}	69.0	161 ± 5	0.73 ± 0.04
XRR 050410	49.5	-1.65 ± 0.08	94 ± 4	78.5	74^{+19}_{-9}	24^{+13}_{-8}	61.3	42 ± 2	0.78 ± 0.06
XRR 050525A	12.8	-1.76	1350	166.4	82^{+4}_{-3}	274^{+20}_{-27}	17.9	153 ± 2	0.85
XRR 050713A	190.7	-1.54 ± 0.08	28 ± 1	70.8	421^{+117}_{-80}	BAT/KW ^g	51 ± 2	0.72 ± 0.05
XRR 050815	3.2	-1.8 ± 0.2	32 ± 6	75.6	43^{+9}_{-6}	130^{+1390}_{-111}	62.1	0.8 ± 0.1	0.9 ± 0.2
XRR 050915B	56.7	-1.90 ± 0.06	67 ± 2	55.5	61^{+7}_{-4}	12^{+3}_{-3}	46.0	33.8 ± 1.4	0.93 ± 0.05
XRR 051021B	59.6	-1.55 ± 0.14	16 ± 1	56.9	72^{+45}_{-13}	5^{+7}_{-3}	49.7	8.4 ± 0.9	0.73 ± 0.10
XRR 060111A	18.2	-1.65 ± 0.07	75 ± 3	69.0	74^{+19}_{-10}	17^{+8}_{-5}	50.4	12.0 ± 0.6	0.78 ± 0.05
XRR 060115	157.3	-1.7 ± 0.1	13 ± 1	52.6	63^{+16}_{-10}	3^{+3}_{-2}	45.8	17.1 ± 1.5	0.84 ± 0.09
XRR 060206	12.6	-1.71 ± 0.08	74 ± 3	64.6	78^{+38}_{-13}	14^{+6}_{-4}	55.3	8.3 ± 0.4	0.82 ± 0.06
XRR 060211A	143.2	-1.8 ± 0.1	13 ± 1	71.5	58^{+18}_{-8}	4^{+4}_{-2}	60.6	15.7 ± 1.4	0.85 ± 0.10
XRR 060510A	23.7	-1.57 ± 0.07	362 ± 13	54.0	184^{+36}_{-24}	KW ^j	80.5 ± 3.1	0.74 ± 0.05
XRR 060707	74.4	-1.7 ± 0.1	25 ± 2	70.5	63^{+21}_{-10}	9^{+10}_{-4}	60.5	16.0 ± 1.5	0.8 ± 0.1
XRR 060814	230.3	-1.53 ± 0.03	67 ± 1	30.1	257^{+122}_{-58}	KW ^k	146 ± 2	0.72 ± 0.02
XRR 060825	10.6	-1.72 ± 0.07	103 ± 4	64.8	73^{+28}_{-11}	20^{+9}_{-6}	53.7	9.6 ± 0.5	0.83 ± 0.05
XRR 060904A	132.5	-1.55 ± 0.04	62 ± 1	43.6	163 ± 31	KW ^l	77.2 ± 1.5	0.73 ± 0.02
XRR 060927	24.7	-1.65 ± 0.08	52 ± 2	70.4	72^{+25}_{-11}	12^{+7}_{-4}	57.5	11.3 ± 0.7	0.78 ± 0.06

TABLE 1—Continued

GRB	PL				CPL				OTHER			
	T_{100}^{BATa}	Γ	K_{50}^{d}	χ^2_{e}	$E_{\text{peak}}^{\text{obs}}$ (keV)	$(10^{-3} \text{ photons cm}^{-2} \text{ s}^{-1} \text{ keV}^{-1})$	K_{50}^{g}	χ^2_{e}	$E_{\text{peak}}^{\text{f}}$	Mo/Inst ^h	$S(15\text{--}150 \text{ keV})^{\text{b}}$	SR23 ^e
GRB 050124.....	6.0	-1.47 ± 0.08	213 ± 11	58.7	95 ⁺³⁹ ₋₁₆	47 ⁺²³ ₋₁₅	45.4	11.9 ± 0.7	0.69 ± 0.06
GRB 050128.....	30.4	-1.37 ± 0.07	172 ± 7	59.3	113 ⁺⁴⁶ ₋₁₉	35 ⁺¹⁴ ₋₁₀	44.8	50.2 ± 2.3	0.65 ± 0.05
GRB 050219A.....	35.1	-1.31 ± 0.06	123 ± 4	103.2	92 ⁺¹² ₋₈	41 ⁺¹³ ₋₁₀	45.5	41.1 ± 1.6	0.62 ± 0.03
GRB 050326.....	41.0	-1.25 ± 0.04	216 ± 4	42.1	201 ± 24	KW ^m	88.6 ± 1.6	0.59 ± 0.02
GRB 050401.....	36.8	-1.40 ± 0.07	231 ± 9	37.1	132 ± 16	KW ⁿ	82.2 ± 3.1	0.66 ± 0.04
GRB 050603.....	21.4	-1.16 ± 0.06	289 ± 10	71.1	349 ± 28	KW ^o	63.6 ± 2.3	0.56 ± 0.03
GRB 050716.....	90.1	-1.37 ± 0.06	72 ± 3	52.5	123 ⁺⁶¹ ₋₂₄	13 ⁺⁴ ₋₃	39.4	61.7 ± 2.4	0.65 ± 0.04
GRB 050717.....	209.2	-1.30 ± 0.05	31 ± 1	48.5	210 ⁺¹⁹³⁴ ₋₈₃₀	BAT/KW ^p	63.1 ± 1.8	0.61 ± 0.03
GRB 050922C.....	6.8	-1.37 ± 0.06	247 ± 8	44.9	131 ⁺⁵¹ ₋₂₄	HETE ^q	16.2 ± 0.5	0.65 ± 0.03
GRB 051109A.....	45.4	-1.5 ± 0.2	51 ± 6	63.7	161 ⁺²²⁴ ₋₅₈	KW ^r	22.0 ± 2.7	0.7 ± 0.1
GRB 060105.....	87.6	-1.07 ± 0.04	191 ± 4	32.5	424 ⁺²⁵ ₋₂₀	KW ^s	176 ± 3	0.53 ± 0.02
GRB 060204B.....	195.0	-1.44 ± 0.09	17 ± 1	47.0	100 ⁺⁷⁵ ₋₁₇	3 ± 2	38.9	29.5 ± 1.8	0.68 ± 0.05
GRB 060813.....	36.7	-1.36 ± 0.04	155 ± 3	54.1	168 ⁺¹⁷ ₋₃₉	22 ⁺⁵ ₋₄	43.5	54.6 ± 1.4	0.64 ± 0.03
GRB 060908.....	28.5	-1.35 ± 0.06	103 ± 3	50.7	150 ⁺¹⁸⁴ ₋₄₁	15 ⁺⁵ ₋₃	44.2	28.0 ± 1.1	0.63 ± 0.04

^a In seconds.^b BAT 15–150 keV energy fluence in 10^{-7} ergs $\text{cm}^{-2} \text{ s}^{-1}$ with the BAT best-fit model.^c A fluence ratio of $S(25\text{--}50 \text{ keV})/S(50\text{--}100 \text{ keV})$ derived from a PL fit.^d In 10^{-4} photons $\text{cm}^{-2} \text{ s}^{-1} \text{ keV}^{-1}$.^e The degrees of freedom in a PL fit and a CPL fit are 57 and 56, respectively.^f In keV.^g In 10^{-3} photons $\text{cm}^{-2} \text{ s}^{-1} \text{ keV}^{-1}$.^h Spectral fitting model used/GRB instrument that reports $E_{\text{peak}}^{\text{obs}}$.ⁱ Morris et al. 2007; $E_{\text{peak}}^{\text{obs}}$ derived from a CPL model.^j Golenetskii et al. 2006a, GCN Circ. 5113. $E_{\text{peak}}^{\text{obs}}$ derived from a CPL model.^k Golenetskii et al. 2006c, GCN Circ. 5460. $E_{\text{peak}}^{\text{obs}}$ derived from a CPL model.^l Golenetskii et al. 2006d, GCN Circ. 5518. $E_{\text{peak}}^{\text{obs}}$ derived from a Band model.^m Golenetskii et al. 2005a, GCN Circ. 3152. $E_{\text{peak}}^{\text{obs}}$ derived from a Band model.ⁿ Golenetskii et al. 2005b, GCN Circ. 3179. $E_{\text{peak}}^{\text{obs}}$ derived from a Band model for the first episode.^o Golenetskii et al. 2005c, GCN Circ. 3518. $E_{\text{peak}}^{\text{obs}}$ derived from a Band model.^p Krimm et al. 2006; $E_{\text{peak}}^{\text{obs}}$ derived from a CPL model.^q Crew et al. 2005, GCN Circ. 4021. $E_{\text{peak}}^{\text{obs}}$ derived from a CPL model.^r Golenetskii et al. 2005d, GCN Circ. 4238. $E_{\text{peak}}^{\text{obs}}$ derived from a CPL model.^s Tashiro et al. 2007; $E_{\text{peak}}^{\text{obs}}$ derived from a CPL model.

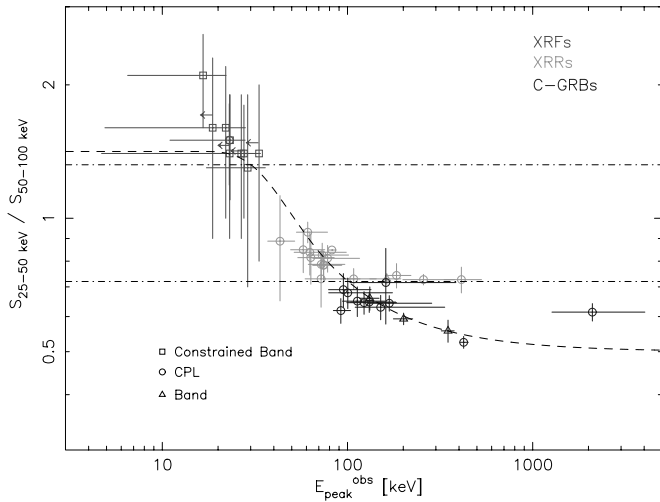


FIG. 4.— $S(25-50 \text{ keV})/S(50-100 \text{ keV})$ fluence ratios and $E_{\text{peak}}^{\text{obs}}$ values of BAT-detected bursts. The dashed line shows the fluence ratios as a function of $E_{\text{peak}}^{\text{obs}}$ assuming $\Gamma_1 = -1$ and $\Gamma_2 = -2.5$ in the Band function. The dash-dotted lines indicate the boundaries between XRFs, XRRs, and C-GRBs (eq. [1] in the text). [See the electronic edition of the Journal for a color version of this figure.]

parameters by *Konus-Wind* (Golenetskii et al. 2006b). Based on these selection criteria, a total of 41 GRBs are selected, including 10 XRFs, 17 XRRs, and 14 C-GRBs.

3. PROMPT EMISSION

The spectral properties of the prompt emission for our 41 GRBs are summarized in Table 1. Figure 4 shows the $S(25-50 \text{ keV})/S(50-100 \text{ keV})$ fluence ratio versus $E_{\text{peak}}^{\text{obs}}$. As seen in the figure, $E_{\text{peak}}^{\text{obs}}$ of the BAT GRBs ranges from a few tens of keV to a few hundreds of keV. This broad continuous distribution of $E_{\text{peak}}^{\text{obs}}$ is consistent with the *BeppoSAX* (Kippen et al. 2003) and *HETE-2* (Barraud et al. 2003; Sakamoto et al. 2005) results. The BAT GRBs follow well on the curve calculated assuming $\Gamma_1 = -1$ and $\Gamma_2 = -2.5$ for the Band function. The gap in the $S(25-50 \text{ keV})/S(50-100 \text{ keV})$ fluence ratio from 0.8 to 1.2 in our sample is likely due to a selection effect. Essentially, we selected bursts based on the measurement of $E_{\text{peak}}^{\text{obs}}$ for XRRs and C-GRBs. This criterion is more or less equivalent to selecting the bursts based on their brightness. On the other hand, most of the XRFs were selected

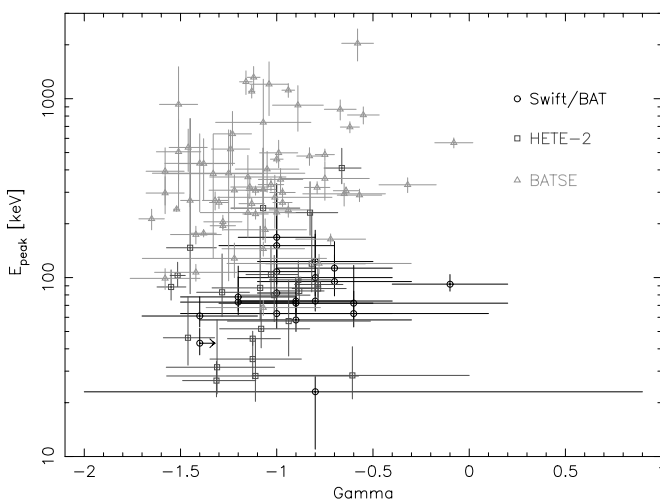


FIG. 5.— Distribution of the low-energy photon index Γ and $E_{\text{peak}}^{\text{obs}}$ in a CPL model. The samples of BAT, *HETE-2*, and BATSE are shown as circles, squares, and triangles, respectively. [See the electronic edition of the Journal for a color version of this figure.]

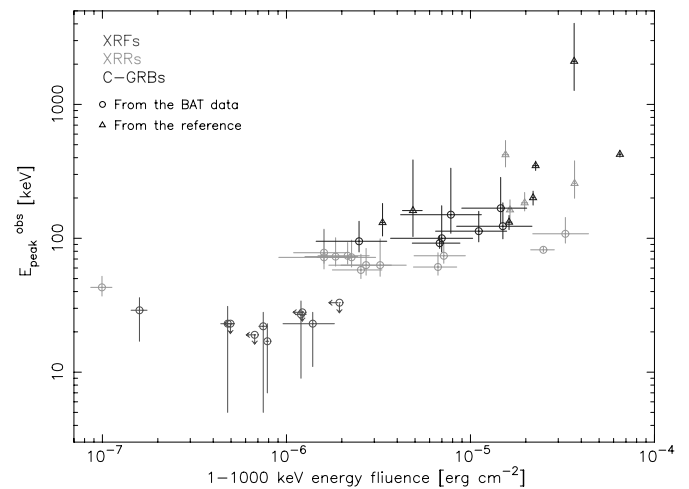
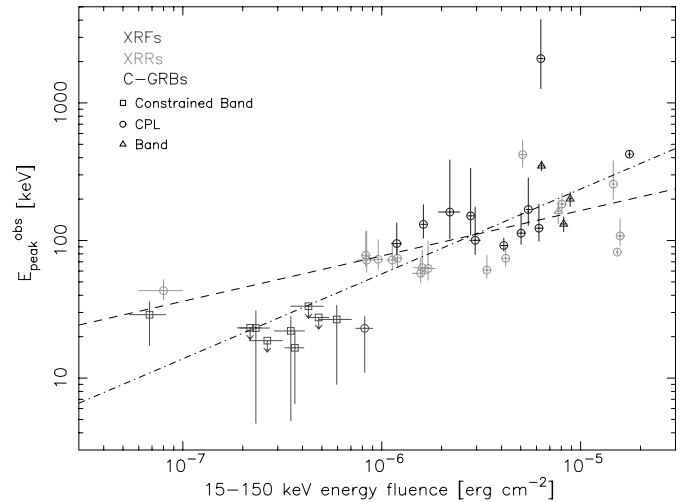


FIG. 6.— Plot of the 15–150 keV fluence and peak spectral energy $E_{\text{peak}}^{\text{obs}}$ of XRFs, XRRs, and C-GRBs detected by BAT. The dashed and dash-dotted lines are the best fits to the data with and without taking into account the errors, and they are given by $\log(E_{\text{peak}}^{\text{obs}}) = 3.87_{-0.16}^{+0.33} + (0.33 \pm 0.13) \log[S(15-150 \text{ keV})]$ and $\log(E_{\text{peak}}^{\text{obs}}) = (5.46 \pm 0.80) + (0.62 \pm 0.14) \log[S(15-150 \text{ keV})]$. Those bursts for which $E_{\text{peak}}^{\text{obs}}$ is derived from a *constrained* Band function, a CPL, and the Band function are marked as squares, circles, and triangles, respectively. [See the electronic edition of the Journal for a color version of this figure.]

based on the photon index value in a PL fit ($\Gamma < -2$). This is equivalent to selecting by the softness of the bursts. Therefore, there is a different way to distinguish between XRFs, and XRRs and C-GRBs. Evidently, as shown in Figure 3, there is no such gap in the histogram of the fluence ratios for the BAT GRBs if the whole burst sample has been examined. Therefore, we believe that the gap in the fluence ratio at 0.8–1.2 is due to the way in which we selected the bursts.

In Figure 5, we compare $E_{\text{peak}}^{\text{obs}}$ in a CPL fit and the low-energy photon indices Γ for the BAT, *HETE-2*, and BATSE samples. For both the *HETE-2* (Sakamoto et al. 2005) and the BATSE (Kaneko et al. 2006) samples, we only plotted GRBs with a CPL model as the best representative model for the time-averaged spectrum to reduce the systematic differences in both Γ and $E_{\text{peak}}^{\text{obs}}$ due to the different choices of spectral models (Kaneko et al. 2006). As seen in the figure, the range of Γ -values derived from the BAT data alone are consistent with the *HETE-2* and BATSE results. In addition, we have confirmed that the Γ -values for XRFs and XRRs (GRBs with $E_{\text{peak}}^{\text{obs}} < 100 \text{ keV}$) cover the same range as for C-GRBs (GRBs with $E_{\text{peak}}^{\text{obs}} > 100 \text{ keV}$; Sakamoto et al. 2005).

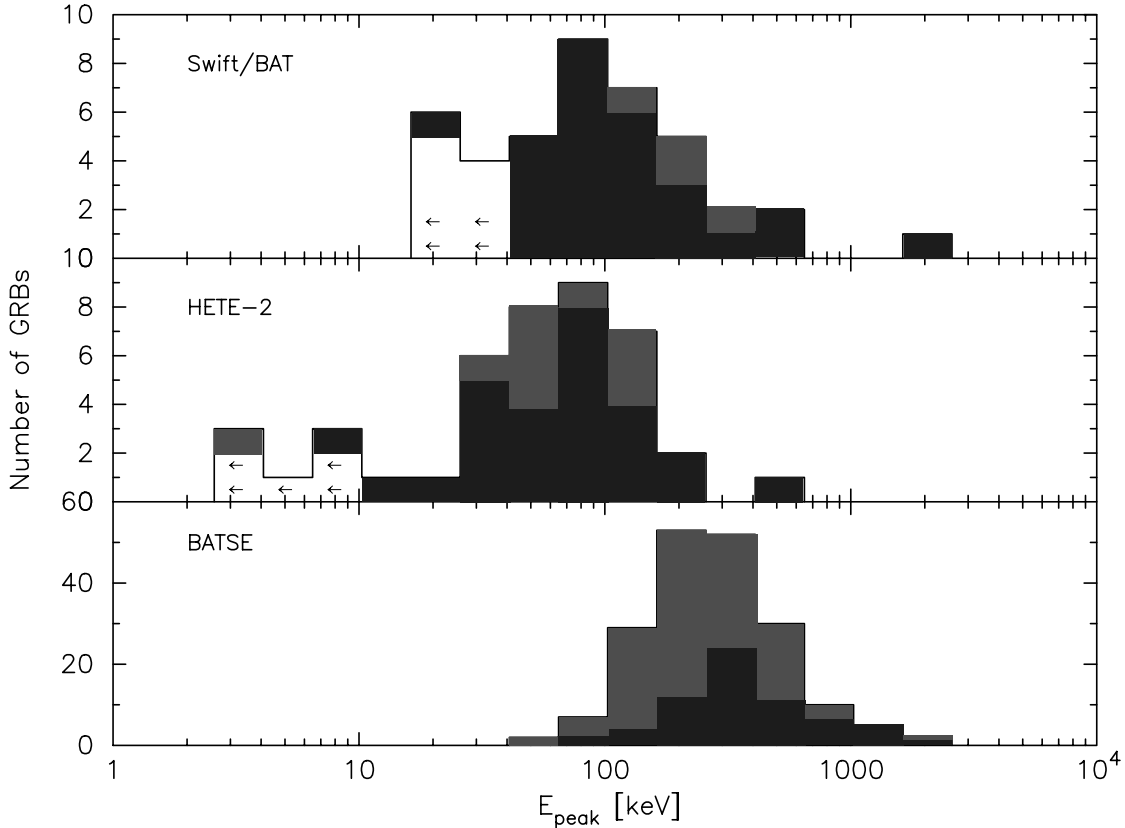


FIG. 7.— Distribution of E_{peak} for the *Swift*/BAT, *HETE*-2, and BATSE samples. The white, gray, and black histograms represent E_{peak} derived by the *constrained* Band function, a CPL model, and the Band function, respectively. The left-side arrows are E_{peak} with upper limits. [See the electronic edition of the *Journal* for a color version of this figure.]

The top panel of Figure 6 shows $E_{\text{peak}}^{\text{obs}}$ and the 15–150 keV fluence, $S(15\text{--}150\text{ keV})$, for the BAT GRBs. We note a correlation between $E_{\text{peak}}^{\text{obs}}$ and $S(15\text{--}150\text{ keV})$. For the purpose of the correlation study, we assigned the median of the 90% confidence interval to be the best-fit value of $E_{\text{peak}}^{\text{obs}}$, so that the errors would be symmetric. For cases in which we only have upper limits for E_{peak} , we assigned the best-fit values of E_{peak} to be the median of 0 and 90% upper limit, and we assigned the symmetric error to be half that value. The linear correlation coefficient between $\log[S(15\text{--}150\text{ keV})]$ and $\log(E_{\text{peak}}^{\text{obs}})$ is $+0.76$ for a sample of 41 GRBs using the best-fit values.

The best-fit functions with and without taking into account the errors are $\log(E_{\text{peak}}^{\text{obs}}) = 3.87_{-0.16}^{+0.33} + (0.33 \pm 0.03) \log[S(15\text{--}150\text{ keV})]$ and $\log(E_{\text{peak}}^{\text{obs}}) = (5.46 \pm 0.80) + (0.62 \pm 0.14) \log[S(15\text{--}150\text{ keV})]$, respectively.

Since the fluence in the 15–150 keV band is not a good quantity to examine the correlation with $E_{\text{peak}}^{\text{obs}}$ because of its narrow energy range of integration, we also investigate the correlation between $E_{\text{peak}}^{\text{obs}}$ and the fluence in the 1–1000 keV band, $S(1\text{--}1000\text{ keV})$. For GRBs that have the measurement of $E_{\text{peak}}^{\text{obs}}$ from BAT data alone, we calculate $S(1\text{--}1000\text{ keV})$ directly from a spectral fitting process using the Band function. Therefore, uncertainty in the spectral parameters in the Band function, especially in the high-energy photon index Γ_2 is also taken into account in an error calculation of the fluence. For GRBs for which we use E_{peak} from the literature, we calculated the fluence using the spectral parameters presented in the literature, and the error associated in the normalization of the best-fit spectral model is used to calculate an error of the fluence. If the reported best-fit model is a CPL for these GRBs, we use $\Gamma_2 = -2.3$ to calculate the fluence in the Band function. The

bottom panel of Figure 6 shows the distribution between $E_{\text{peak}}^{\text{obs}}$ and $S(1\text{--}1000\text{ keV})$.

To take into account the errors associated with $E_{\text{peak}}^{\text{obs}}$ and $S(1\text{--}1000\text{ keV})$ in our calculation of the correlation coefficient, we generate 10,000 random numbers assuming a Gaussian distribution in $E_{\text{peak}}^{\text{obs}}$ and $S(1\text{--}1000\text{ keV})$ of the central value and the error for each GRB in the sample. For GRBs only having the upper limits in $E_{\text{peak}}^{\text{obs}}$ and/or $S(1\text{--}1000\text{ keV})$, we use a uniform distribution to generate the random numbers. Then we calculate the linear correlation coefficient for the 10,000 burst sample in $\log[E_{\text{peak}}^{\text{obs}}] - \log[S(1\text{--}1000\text{ keV})]$ space and make a histogram of the calculated correlation coefficient. The highest peak and 68% points from the highest value of the histogram are assigned as the central value and 1σ interval of the correlation coefficient. We investigate the correlation coefficient for (1) GRBs with $E_{\text{peak}}^{\text{obs}}$ from a CPL model (sample A; total 32 GRBs); (2) GRBs with a constrained $E_{\text{peak}}^{\text{obs}}$ from a C-Band model and a CPL model (sample B; total 37 GRBs); and (3) all 41 GRBs (sample C) to evaluate the systematic effect of $E_{\text{peak}}^{\text{obs}}$ due to the different spectral models (C-Band vs. CPL). The calculated correlation coefficients are $+0.50_{-0.12}^{+0.11}$, $+0.63_{-0.10}^{+0.08}$, and $+0.68_{-0.08}^{+0.07}$ (all in 1σ error) for samples A, B, and C, respectively. The probabilities of such a correlation occurring by chance in each sample size are 3.4×10^{-2} – 2.4×10^{-4} , 5.8×10^{-4} – 5.3×10^{-7} , and 4.1×10^{-5} – 2.3×10^{-8} in the 1σ interval for samples A, B, and C, respectively. Thus, the correlation between $E_{\text{peak}}^{\text{obs}}$ and the fluence is still significant even if we use the fluence in the 1–1000 keV band and also take into account the $E_{\text{peak}}^{\text{obs}}$ derived by the different spectral models.

The histograms of $E_{\text{peak}}^{\text{obs}}$ for the *Swift*/BAT, *HETE*-2 (Sakamoto et al. 2005), and BATSE (Kaneko et al. 2006) samples are shown in

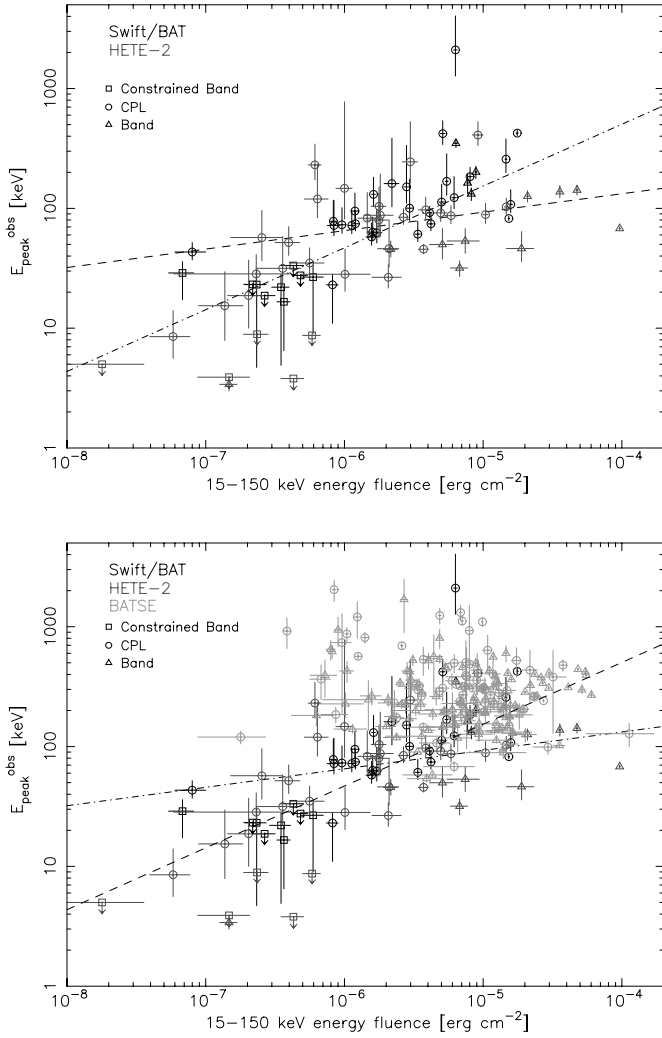


FIG. 8.—*Top*: Plot of the 15–150 keV fluence and peak spectral energy $E_{\text{peak}}^{\text{obs}}$ for BAT and *HETE-2* samples. *Bottom*: Plot of the 15–150 keV fluence and peak spectral energy $E_{\text{peak}}^{\text{obs}}$ for BAT, *HETE-2*, and BATSE samples. The dashed and dash-dotted line are the best fit to the BAT and the *HETE-2* data with and without taking into account the errors, and they are given by $\log(E_{\text{peak}}^{\text{obs}}) = 2.74_{-0.08}^{+0.15} + (0.15 \pm 0.02) \log[S(15-150 \text{ keV})]$ and $\log(E_{\text{peak}}^{\text{obs}}) = (4.77 \pm 0.63) + (0.52 \pm 0.11) \log[S(15-150 \text{ keV})]$. [See the electronic edition of the *Journal* for a color version of this figure.]

Figure 7. We notice a difference in the distributions of $E_{\text{peak}}^{\text{obs}}$ for the three GRB instruments, especially between the BAT (or the *HETE-2*) and the BATSE distributions. Applying the two-sample Kolmogorov-Smirnov (K-S) test to the $E_{\text{peak}}^{\text{obs}}$ distributions for the BAT and *HETE-2* samples, the BAT and BATSE samples, and the *HETE-2* and BATSE samples, we find K-S test probabilities of 0.44, 2.3×10^{-9} , and 4.1×10^{-16} , respectively. Based on these tests, we may conclude that the BATSE GRB samples have a systematically higher $E_{\text{peak}}^{\text{obs}}$ than the BAT and the *HETE-2* samples. This is probably because not only is the BATSE energy range higher than those other instruments, but also the current BATSE spectral catalog only contains the bright GRBs, therefore systematically selecting higher $E_{\text{peak}}^{\text{obs}}$ GRBs in the catalog (Kaneko et al. 2006).

Figure 8 shows $E_{\text{peak}}^{\text{obs}}$ and $S(15-150 \text{ keV})$ of the BAT, *HETE-2*, and BATSE samples. The fluence in the 15–150 keV band for the *HETE-2* and BATSE samples is calculated using the best-fit spectral model reported in the catalog (Sakamoto et al. 2005; Kaneko et al. 2006). The error in the fluence for the *HETE-2* and BATSE

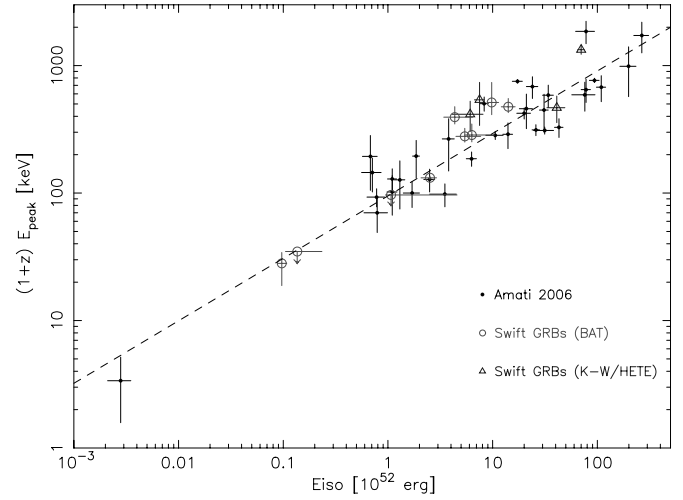


FIG. 9.—Isotropic equivalent energy, E_{iso} vs. the peak energy in the GRB rest frame, E_{peak} for the known redshift BAT GRBs in this work (circles), pre-*Swift* GRBs (dots) and the known redshift *Swift* GRBs observed by *Konus-Wind* or *HETE-2* (triangles). The dashed line is the best-fit correlation reported by Amati (2006) ($E_{\text{peak}}^{\text{src}} = 95 \text{ keV} [E_{\text{iso}} / (10^{52} \text{ ergs})]^{0.49}$). [See the electronic edition of the *Journal* for a color version of this figure.]

samples is calculated by scaling the error in the normalization of the best-fit spectral model. As clearly seen in the figure, $S(15-150 \text{ keV})$ and $E_{\text{peak}}^{\text{obs}}$ of the BAT GRBs are consistent with both the *HETE-2* and the BATSE samples. The strong correlation between $E_{\text{peak}}^{\text{obs}}$ and $S(15-150 \text{ keV})$ still exists by combining the BAT and the *HETE-2* samples. The correlation coefficient combining the BAT and *HETE-2* GRBs is +0.685 for 83 samples. The probability of such a correlation occurring by chance is $< 10^{-11}$. The best-fit correlation functions between $E_{\text{peak}}^{\text{obs}}$ and $S(15-150 \text{ keV})$ with and without taking into account the errors are $\log(E_{\text{peak}}^{\text{obs}}) = 2.74_{-0.08}^{+1.51} + (0.15 \pm 0.02) \log[S(15-150 \text{ keV})]$ and $\log(E_{\text{peak}}^{\text{obs}}) = (4.77 \pm 0.63) + (0.52 \pm 0.11) \log[S(15-150 \text{ keV})]$, respectively. However, as clearly shown in both Figures 7 and 8, the BAT XRFs are not softer (or weaker) than the *HETE-2* sample. This is because of the higher observed energy band of the BAT compared to that of the *HETE-2* Wide-field X-ray Monitor (WXM; 2–25 keV) (Shirasaki et al. 2003). Thus, caution might be needed when comparing the BAT and *HETE-2* XRF samples. It is also clear from the figures that the $E_{\text{peak}}^{\text{obs}}$ distribution of the

TABLE 2
 $E_{\text{peak}}^{\text{src}}$ AND E_{iso} DERIVED FROM THE BAT DATA

GRB	z	$E_{\text{peak}}^{\text{src}}$ (keV)	E_{iso} (10^{52} ergs)	Instrument
050401 ¹	2.9	467 \pm 110	41 \pm 8	<i>Konus-Wind</i>
050416A	0.6535	28 ⁺⁶ ₋₉	0.096 ^{+0.011} _{-0.009}	BAT
050525A	0.606	131 ⁺⁴ ₋₃	2.5 ^{+0.4} _{-0.5}	BAT
050603 ^a	2.821	1333 \pm 107	70 \pm 5	<i>Konus-Wind</i>
050824	0.83	<35	0.13 ^{+0.10} _{-0.03}	BAT
050922C ^a	2.198	415 \pm 111	6.1 \pm 2.0	<i>HETE-2</i>
051109A ^a	2.346	539 \pm 200	7.5 \pm 0.8	<i>Konus-Wind</i>
060115	3.53	285 ⁺⁶³ ₋₃₄	6.3 ^{+4.1} _{-0.9}	BAT
060206	4.048	394 ⁺⁸² ₋₄₆	4.3 ^{+2.1} _{-0.9}	BAT
060707	3.425	279 ⁺⁴³ ₋₂₈	5.4 ^{+2.3} _{-1.0}	BAT
060908 ^b	2.43	514 ⁺²²⁴ ₋₁₀₂	9.8 ^{+1.6} _{-0.9}	BAT
060926	3.20	<96.6	1.1 ^{+3.5} _{-0.1}	BAT
060927	5.6	475 ⁺⁷⁷ ₋₄₇	14.1 ^{+2.3} _{-2.0}	BAT

NOTE.—The uncertainty is 1σ .

^a $E_{\text{peak}}^{\text{src}}$ and E_{iso} values from Amati (2006).

^b The high-energy photon index Γ_2 of the Band function is fixed at -2.3 .

TABLE 3
XRT X-RAY SPECTRAL PROPERTIES OF 41 SWIFT BURSTS

GRB	WT					PC				
	t_{start} (s)	t_{stop} (s)	N_{H} (10^{21} cm^{-2})	Γ^a	χ^2/dof	t_{start} (s)	t_{stop} (s)	N_{H} (10^{21} cm^{-2})	Γ^a	χ^2/dof
XRF 050406	92	1.5×10^5	...	-2.3	32.0/16	1.1×10^4	1.4×10^6	$3.5^{+5.9}_{-2.0}$	$-3.5^{+1.1}_{-2.3}$	6.3/8
XRF 050416A.....	85	1.4×10^5	<11	$-2.4^{+0.8}_{-1.5}$	9.9/9	184	6.4×10^6	$5.6^{+1.0}_{-0.9}$	-2.1 ± 0.1	81.4/100
XRF 050714B.....	157	219	$7.2^{+1.2}_{+1.0}$	$-5.8^{+0.5}_{-0.6}$	34.2/27	257	9.5×10^5	$2.9^{+1.0}_{-0.8}$	$-2.8^{+0.3}_{-0.4}$	21.9/17
XRF 050819	147	202	<0.4	$-2.3^{+0.2}_{-0.3}$	7.3/10	239	6.3×10^5	<2	$-2.2^{+0.3}_{-0.4}$	17.7/11
XRF 050824	6.2×10^3	2.1×10^6	$2.4^{+1.0}_{-0.9}$	-2.2 ± 0.2	29.4/39
XRF 060219	126	5.7×10^4	$3.2^{+6.9}_{-2.9}$	<-2.6	8.3/9	146	6.9×10^5	$3.2^{+1.1}_{-0.9}$	$-3.1^{+0.4}_{-0.5}$	23.4/19
XRF 060428B.....	212	418	0.3 ± 0.1	-2.8 ± 0.1	126.9/121	622	1.0×10^6	<0.2	-1.9 ± 0.1	17.2/30
XRF 060512	110	155	$0.6^{+0.7}_{-0.5}$	$-4.4^{+0.6}_{-0.7}$	13.9/10	3.7×10^3	3.5×10^5	<0.3	$-1.9^{+0.1}_{-0.2}$	24.6/15
XRF 060923B.....	139	6.0×10^3	3^{+2}_{-1}	$-2.0^{+0.4}_{-0.5}$	2.6/8
XRF 060926	66	875	25^{+28}_{-17}	$-1.9^{+0.2}_{-0.3}$	11.4/15	4.3×10^3	2.8×10^5	<40	$-1.8^{+0.2}_{-0.4}$	10.0/7
XRR 050219B.....	3.2×10^3	1.2×10^5	0.6 ± 0.2	$-1.81^{+0.08}_{-0.09}$	152.6/161	9.1×10^3	3.2×10^6	$1.0^{+0.6}_{-0.5}$	-2.0 ± 0.2	26.6/22
XRR 050410.....	1.9×10^3	7.9×10^4	13^{+18}_{-9}	<-3.3	28.7/26	1.9×10^3	9.2×10^5	<8	$-1.7^{+0.5}_{-1.0}$	23.1/13
XRR 050525A.....	5.9×10^3	3.0×10^6	2 ± 1	-2.1 ± 0.2	31.8/41
XRR 050713A.....	80	1.2×10^4	2.4 ± 0.3	$-2.41^{+0.08}_{-0.09}$	146.5/166	4.3×10^3	1.7×10^6	2.5 ± 0.5	-2.1 ± 0.1	57.6/78
XRR 050815.....	89	1.8×10^5	<2	$-1.8^{+0.3}_{-0.4}$	9.7/11
XRR 050915B.....	150	6.5×10^4	<0.5	$-2.6^{+0.1}_{-0.2}$	53.7/53	288	9.6×10^5	<1	$-2.2^{+0.2}_{-0.3}$	25.7/24
XRR 051021B.....	86	115	<10	$-1.2^{+0.5}_{-1.1}$	1.6/2	258	5.2×10^5	<4	$-2.0^{+0.2}_{-0.4}$	9.1/14
XRR 060111A.....	74	517	1.7 ± 0.1	$-2.33^{+0.04}_{-0.05}$	367.6/300	3.8×10^3	7.6×10^5	$1.4^{+0.5}_{-0.4}$	-2.2 ± 0.2	33.7/39
XRR 060115.....	121	5.4×10^3	<10	$-1.84^{+0.08}_{-0.09}$	78.9/85	616	4.6×10^5	<8	$-2.3^{+0.1}_{-0.2}$	21.6/26
XRR 060206.....	64	3.7×10^4	14^{+8}_{-7}	$-2.4^{+0.1}_{-0.2}$	72.3/79	1.7×10^3	3.7×10^6	12^{+11}_{-10}	$-2.0^{+0.1}_{-0.2}$	46.5/45
XRR 060211A.....	172	379	0.6 ± 0.2	-1.95 ± 0.07	162.1/172	662	5.7×10^5	$1.3^{+0.8}_{-0.7}$	-2.1 ± 0.2	16.2/23
XRR 060510A.....	98	143	...	-3.7	25.5/8	2.4×10^4	5.7×10^5	<0.4	$-2.03^{+0.06}_{-0.10}$	121.1/100
XRR 060707.....	127	160	<6	$-1.8^{+0.2}_{-0.3}$	6.6/5	488	2.8×10^6	10 ± 7	-2.1 ± 0.1	33.6/39
XRR 060814.....	163	5.2×10^4	2.6 ± 0.2	-2.01 ± 0.05	363.1/280	1.1×10^3	1.4×10^6	3.1 ± 0.3	-2.33 ± 0.08	169.6/158
XRR 060825.....	199	1.1×10^5	<8	$-1.6^{+0.5}_{-1.3}$	5.4/4	92	5.9×10^5	3^{+4}_{-2}	-1.9 ± 0.5	8.9/10
XRR 060904A.....	97	2.1×10^3	$1.8^{+0.2}_{-0.1}$	$-2.61^{+0.07}_{-0.08}$	255.7/208	5.4×10^4	1.3×10^6	3^{+2}_{-1}	$-2.9^{+0.5}_{-0.8}$	10.3/10
XRR 060927.....	147	2.1×10^5	<37	-1.8 ± 0.2	6.7/12
GRB 050124.....	1.1×10^4	5.0×10^6	<0.8	$-1.9^{+0.2}_{-0.3}$	13.0/14
GRB 050128.....	4.5×10^3	9.9×10^4	$0.7^{+0.3}_{-0.2}$	-2.1 ± 0.1	83.6/82
GRB 050219A.....	112	5.7×10^3	$1.8^{+0.5}_{-0.4}$	-2.1 ± 0.2	50.7/55	456	3.2×10^6	<8	$-1.8^{+0.5}_{-1.3}$	6.6/4
GRB 050326.....	3.3×10^3	9.9×10^3	$0.9^{+0.4}_{-0.6}$	$-2.0^{+0.2}_{-0.3}$	22.3/25	5.0×10^3	5.3×10^5	$0.6^{+0.6}_{-0.5}$	-2.0 ± 0.2	27.3/26
GRB 050401.....	133	8.5×10^3	14 ± 2	-1.91 ± 0.04	277.1/266	8.1×10^3	1.1×10^6	21^{+17}_{-11}	-2.0 ± 0.2	22.9/25
GRB 050603.....	3.4×10^4	1.8×10^6	6 ± 4	$-1.98^{+0.12}_{-0.06}$	29.0/49
GRB 050716.....	105	7.6×10^4	<0.1	$-1.34^{+0.03}_{-0.05}$	208.9/202	4.1×10^3	1.8×10^6	0.6 ± 0.5	-2.1 ± 0.2	43.3/36
GRB 050717.....	91	2.7×10^4	$1.8^{+0.7}_{-0.6}$	-1.5 ± 0.1	110.7/105	4000	6.0×10^5	<2	$-1.5^{+0.2}_{-0.3}$	23.6/15
GRB 050922C.....	116	6.2×10^4	<2	-2.02 ± 0.07	107.9/124	3998	5.9×10^5	7 ± 3	$-2.53^{+0.07}_{-0.08}$	60.2/49
GRB 051109A.....	128	1.7×10^4	<4	-2.0 ± 0.1	42.9/32	3.4×10^3	1.5×10^6	5 ± 3	-2.08 ± 0.07	130.7/129
GRB 060105.....	97	4.6×10^3	1.6 ± 0.1	-1.99 ± 0.03	527.6/496	1.0×10^4	3.8×10^5	1.7 ± 0.4	-2.2 ± 0.1	84.8/94
GRB 060204B.....	103	1.8×10^4	1.9 ± 0.2	$-2.28^{+0.08}_{-0.09}$	122.5/129	4.0×10^3	8.1×10^5	1.3 ± 0.3	$-2.3^{+0.1}_{-0.2}$	54.9/56
GRB 060813.....	85	7.6×10^4	1.1 ± 0.4	-1.88 ± 0.08	167.1/163	4.1×10^3	2.6×10^5	1.3 ± 0.4	-2.0 ± 0.1	105.1/102
GRB 060908.....	80	1.3×10^4	<8	-2.3 ± 0.2	18.9/26	1.2×10^3	1.1×10^6	<11	$-2.0^{+0.2}_{-0.3}$	13.7/14

^a The definition of the photon index, Γ , is based on the spectral model: $f(E) = KE^\Gamma$.

BATSE sample is systematically higher compared with the GRB samples of the *HETE-2* and the BAT because of lacking sensitivity below 20 keV for BATSE.

Figure 9 shows the correlation between the peak energy in the GRB rest frame $E_{\text{peak}}^{\text{src}} (\equiv (1+z)E_{\text{peak}}^{\text{obs}})$ and the isotropic radiated energy E_{iso} . We calculated $E_{\text{peak}}^{\text{src}}$ and E_{iso} for the nine known redshift GRBs¹⁸ in our sample using the BAT data (Table 2). For these GRBs, E_{iso} is derived directly from the spectral fitting using the Band function and integrating from 1 keV to 10 MeV at the GRB rest frame. $E_{\text{peak}}^{\text{src}}$ is calculated from $E_{\text{peak}}^{\text{obs}}$ based on a CPL fit. The $E_{\text{peak}}^{\text{src}}$ and E_{iso} values for the remaining *Swift* GRBs are extracted from Amati (2006). The values for the pre-*Swift* GRBs are also extracted from Amati (2006). Although our sample of

known redshift GRBs is small, we have confirmed the existence and the extension of the $E_{\text{peak}}^{\text{src}}-E_{\text{iso}}$ relation to XRFs and XRRs (GRBs with $E_{\text{peak}}^{\text{src}} < 100$ keV) for the *Swift* GRBs (Amati et al. 2002; Lamb et al. 2005; Sakamoto et al. 2004, 2006).

4. X-RAY AFTERGLOW EMISSION

The spectral and temporal properties of the 41 X-ray afterglows are summarized in Tables 3 and 4.

Figure 10 is a composite plot of the X-ray afterglow light curves. Figures 11, 12, and 13 show the light curves in each GRB class. As we subsequently discuss in detail, we find that C-GRBs in our sample tend to have afterglows with shallow decay indices at early times followed by steeper indices at later times and that the breaks between these two indices occur at about 10^3 – 10^4 s. On the other hand, XRF afterglows show a fairly shallow decay index until the

¹⁸ We exclude GRB 060512 because of a less secure measurement of its redshift.

TABLE 4
XRT X-RAY TEMPORAL PROPERTIES OF 41 SWIFT BURSTS

GRB	t_{\min} (s)	t_{\max} (s)	α_1^{inia}	$t_{\text{br}}^{\text{inib}}$ (s)	α_2^{inic}	$\alpha_{2,3}^{\text{fin d}}$	$t_{\text{br}}^{\text{fine}}$ (s)	$\alpha_{3,4}^{\text{fin f}}$	χ^2/dof
XRF 050406	170	1.1×10^6	-1.7 ± 0.3	4360	-0.7 ± 0.2	3.8/4
XRF 050416A.....	90	6.1×10^6	-1.6 ± 0.8	200 ± 90	-0.63 ± 0.04	...	7700 ± 110	-0.86 ± 0.03	86.2/79
XRF 050714B.....	163	8.3×10^5	-7.2 ± 0.7	270 ± 20	-1.1 ± 1.5	...	4100	-0.70 ± 0.07	27.1/15
XRF 050819	154	4.6×10^5	-2.2 ± 2.0	190 ± 20	-5.6 ± 1.0	0.07 ± 0.50	$(2.2 \pm 0.1) \times 10^5$	-1.2 ± 0.6	4.4/5
XRF 050824	6550	2.0×10^6	-0.4 ± 0.1	$(5.9 \pm 2.4) \times 10^4$	-0.87 ± 0.09	36.6/24
XRF 060219	129	3.9×10^5	-4.8 ± 0.8	280 ± 40	-0.4 ± 0.1	...	1700 ± 50	-1.1 ± 0.1	8.5/7
XRF 060428B.....	212	6.4×10^5	-4.4 ± 0.1	670 ± 30	-0.98 ± 0.04	70.3/61
XRF 060512	115	2.9×10^5	-1.30 ± 0.03	14.1/13
XRF 060923B.....	145	5820	-0.60 ± 0.07	6.6/8
XRF 060926	192	2.0×10^5	-0.2 ± 0.2	1500 ± 550	-1.4 ± 0.2	7.8/8
XRR 050219B.....	3200	3.1×10^6	-1.29 ± 0.04	37.1/28
XRR 050410.....	246	6.1×10^5	-0.98 ± 0.09	6.4/4
XRR 050525A.....	77	2.4×10^6	-0.8 ± 0.2	2590	-1.53 ± 0.06	29.6/27
XRR 050713A.....	330	9.2×10^4	-0.18 ± 2.00	1450	-1.05 ± 0.07	...	$(4.5 \pm 0.1) \times 10^4$	-1.9 ± 0.4	36.6/29
XRR 050815.....	3550	1.5×10^5	-1.9 ± 0.3	11.3/9
XRR 050915B.....	151	9.1×10^5	-5.5 ± 0.4	350 ± 35	-1.6 ± 0.4	-0.4 ± 0.2	$(3.4 \pm 0.2) \times 10^4$	-0.9 ± 0.2	33.3/19
XRR 051021B.....	98	4.8×10^5	-1.9 ± 0.1	3310 ± 1720	-0.6 ± 0.2	15.4/14
XRR 060111A.....	3810	7.5×10^5	-0.90 ± 0.04	27.3/27
XRR 060115.....	122	3.6×10^5	-4.4 ± 0.8	150 ± 10	-2.4 ± 0.2	-0.6 ± 0.1	$(3.1 \pm 1.7) \times 10^4$	-1.2 ± 0.2	29.4/30
XRR 060206.....	69	9.1×10^5	-0.4 ± 0.2	1.1×10^4	-1.3 ± 0.1	21.0/12
XRR 060211A.....	186	5.3×10^5	-7 ± 3	-2.1 ± 0.4	2960 ± 1110	-0.60 ± 0.09	72.1/63
XRR 060510A.....	105	5.3×10^5	-3 ± 1	130 ± 8	-0.01 ± 0.06	...	5500 ± 640	-1.48 ± 0.04	161.8/156
XRR 060707.....	207	2.0×10^6	-2.5 ± 0.3	640 ± 100	-0.4 ± 0.1	...	$(2.9 \pm 1.6) \times 10^4$	-1.1 ± 0.1	34.0/25
XRR 060814.....	78	1.1×10^6	-2.56 ± 0.05	940 ± 55	-0.29 ± 0.05	-1.06 ± 0.06	$(4.2 \pm 1.7) \times 10^4$	-1.39 ± 0.07	197.9/185
XRR 060825.....	108	4.1×10^5	-0.96 ± 0.04	10.7/7
XRR 060904A.....	83	1.2×10^6	-3.6 ± 0.2	190 ± 80	-1.1 ± 0.1	40.1/39
XRR 060927.....	93	1.3×10^5	-0.71 ± 0.06	4400 ± 60	-1.9 ± 0.5	8.1/13
GRB 050124.....	1.1×10^4	7.9×10^4	-1.6 ± 0.1	14.0/11
GRB 050128.....	240	7.9×10^4	-0.8 ± 0.1	1700 ± 570	-1.24 ± 0.04	138.7/128
GRB 050219A.....	116	2.4×10^4	-3.2 ± 0.3	256 ± 20	-0.95 ± 0.07	28.0/11
GRB 050326.....	3350	1.9×10^5	-1.70 ± 0.05	15.6/21
GRB 050401.....	136	7.2×10^5	-0.64 ± 0.04	840 ± 60	-0.47 ± 0.05	...	3440 ± 630	-1.4 ± 0.1	126.6/115
GRB 050603.....	3.7×10^4	1.4×10^6	-1.7 ± 0.1	28.5/34
GRB 050716.....	535	1.6×10^6	-1.10 ± 0.04	31.8/34
GRB 050717.....	93	5.4×10^5	-2.0 ± 0.1	320 ± 70	-1.36 ± 0.05	49.8/49
GRB 050922C.....	119	5.4×10^5	-0.8 ± 0.2	280 ± 70	-1.18 ± 0.03	...	$(2.1 \pm 0.7) \times 10^4$	-1.8 ± 0.2	188.6/78
GRB 051109A.....	137	1.5×10^6	-2.9 ± 0.2	2670 ± 300	-0.9 ± 0.2	-1.12 ± 0.07	$(5.2 \pm 1.0) \times 10^4$	-1.38 ± 0.06	179.5/152
GRB 060105.....	97	3.7×10^5	-1.18 ± 0.06	199 ± 2	0.78 ± 0.02	-0.5 ± 0.2	$(5.72 \pm 0.03) \times 10^4$	-2.1 ± 0.2	501.5/438
GRB 060204B.....	450	4.9×10^5	-0.68 ± 0.08	5170 ± 190	-0.02 ± 0.80	...	6670 ± 910	-1.51 ± 0.09	44.4/48
GRB 060813.....	115	1.9×10^5	-0.66 ± 0.05	1680 ± 380	-1.22 ± 0.04	...	$(5.0 \pm 0.5) \times 10^4$	-2.6 ± 0.4	150.5/146
GRB 060908.....	85	9.5×10^5	-0.68 ± 0.06	875 ± 1	-1.62 ± 0.09	...	$(1.3 \pm 0.7) \times 10^4$	-0.8 ± 0.1	51.7/51

^a The decay index of the first power-law component. For most cases, this component corresponds to the very steep decay α_1 as discussed in § 1.

^b The break time of the first component in seconds after the BAT trigger.

^c The postbreak decay power-law index of the first component. For most cases, this component corresponds to the shallow decay α_2 as discussed in § 1.

^d The prebreak decay index of the last component.

^e The break time of the last component in seconds after the BAT trigger. For most cases, this component corresponds to either the shallow decay α_2 or the steeper decay α_3 , as discussed in § 1.

^f The postbreak decay power-law index of the last component. For most cases, this component corresponds to either the steeper decay α_3 or the much steeper decay α_4 , as discussed in § 1.

end of the XRT observation without any significant break. XRRs in our sample were split between these two behaviors, with some manifesting a pattern like the XRF sample and others a pattern like the C-GRB sample.

Figure 14 shows the distribution of best-fit excess neutral hydrogen column densities N_{H} over the Galactic N_{H} (Dickey & Lockman 1990) and photon indices Γ in the PC mode for our sample of bursts. For known redshift GRBs, the excess N_{H} is calculated in the GRB rest frame. Also shown are the *BeppoSAX* values gathered and cited by Frontera (2003) for comparison. There are no systematic differences in N_{H} and Γ between either

the BAT and the pre-*Swift* GRBs or between the individual classes of the BAT GRBs. We also confirmed a significant amount of an excess N_{H} for most of our sample (e.g., Campana et al. 2006; Grupe et al. 2007).

Figure 15 shows the X-ray temporal index in the 0.3–10 keV band taken 1 day after the burst ($\alpha_{1 \text{ day}}$) plotted against $E_{\text{peak}}^{\text{obs}}$ for 36 bursts.¹⁹ There is a systematic trend in $\alpha_{1 \text{ day}}$ of XRFs,

¹⁹ We exclude GRB 050124, GRB 050128, GRB 050219A, GRB 050815, and GRB 060923B for this study because there are no X-ray data around 1 day after the burst.

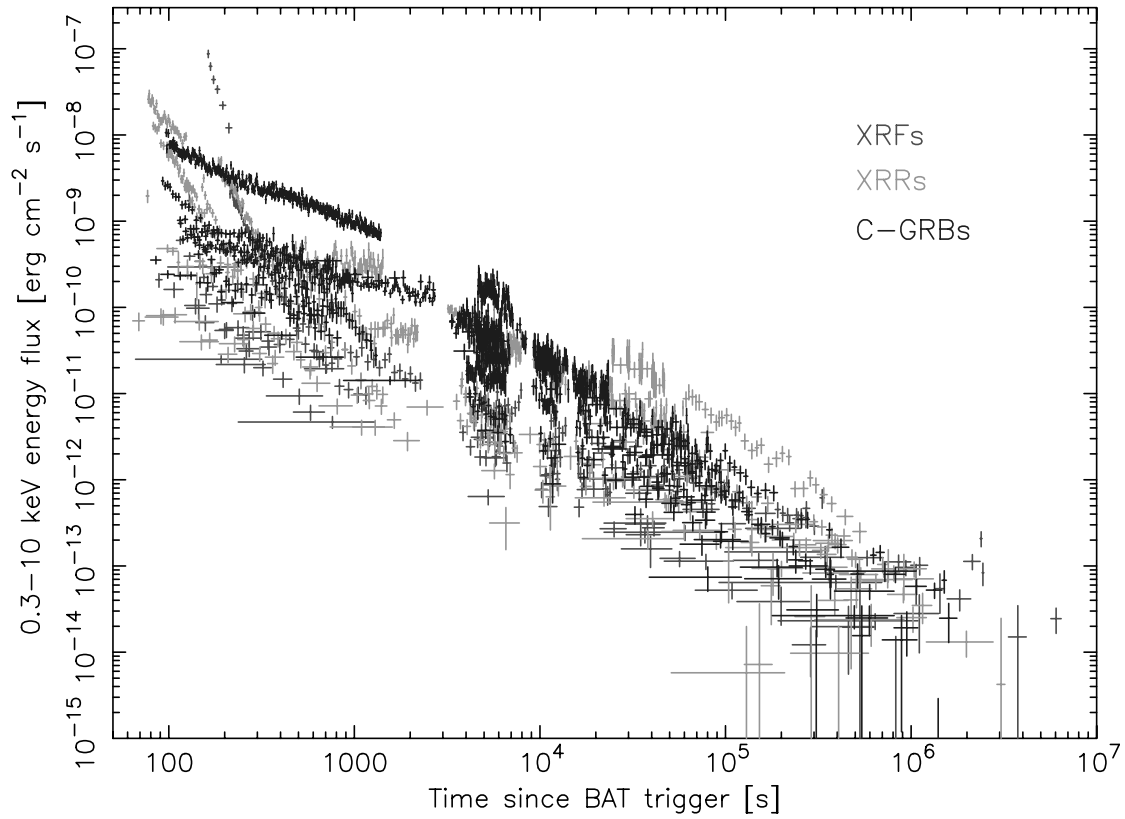


FIG. 10.—Composite plot of the 0.3–10 keV fluxes of the X-ray afterglow light curves of the XRFs, XRRs, and C-GRBs in our sample. [See the electronic edition of the Journal for a color version of this figure.]

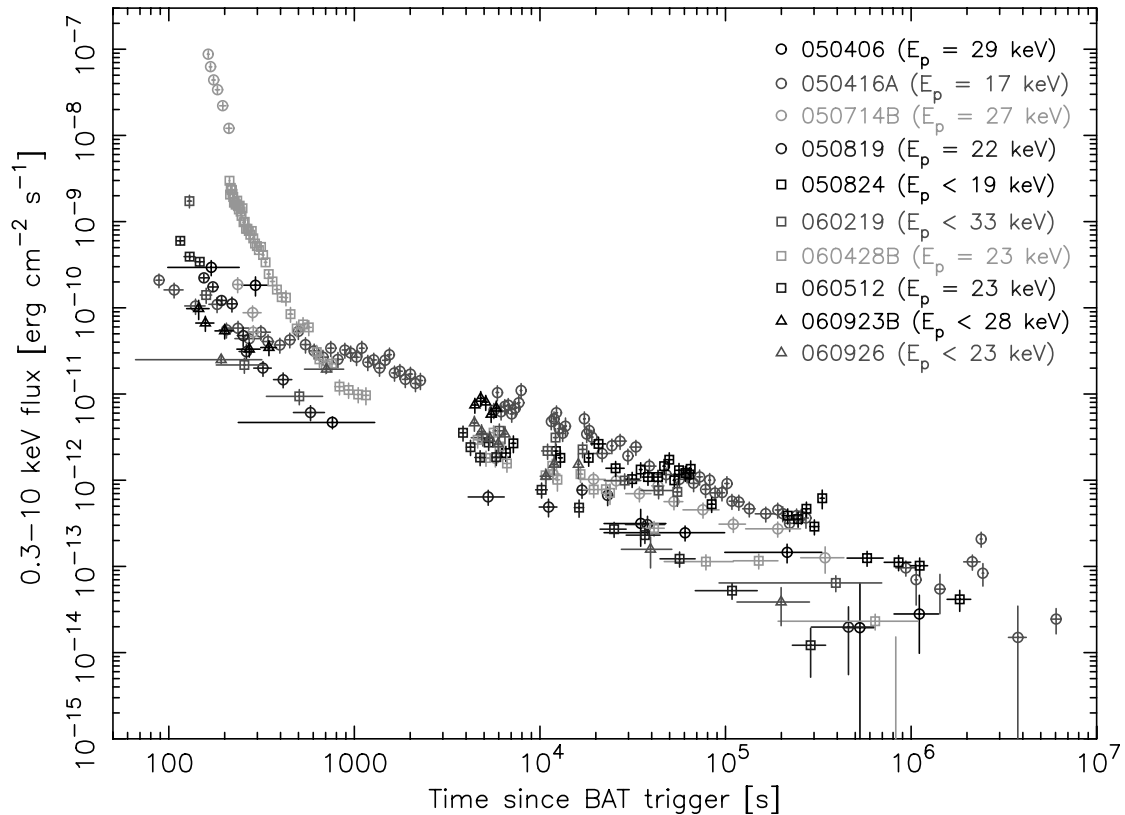


FIG. 11.—Composite plot of the 0.3–10 keV X-ray afterglow light curves of XRFs. [See the electronic edition of the Journal for a color version of this figure.]

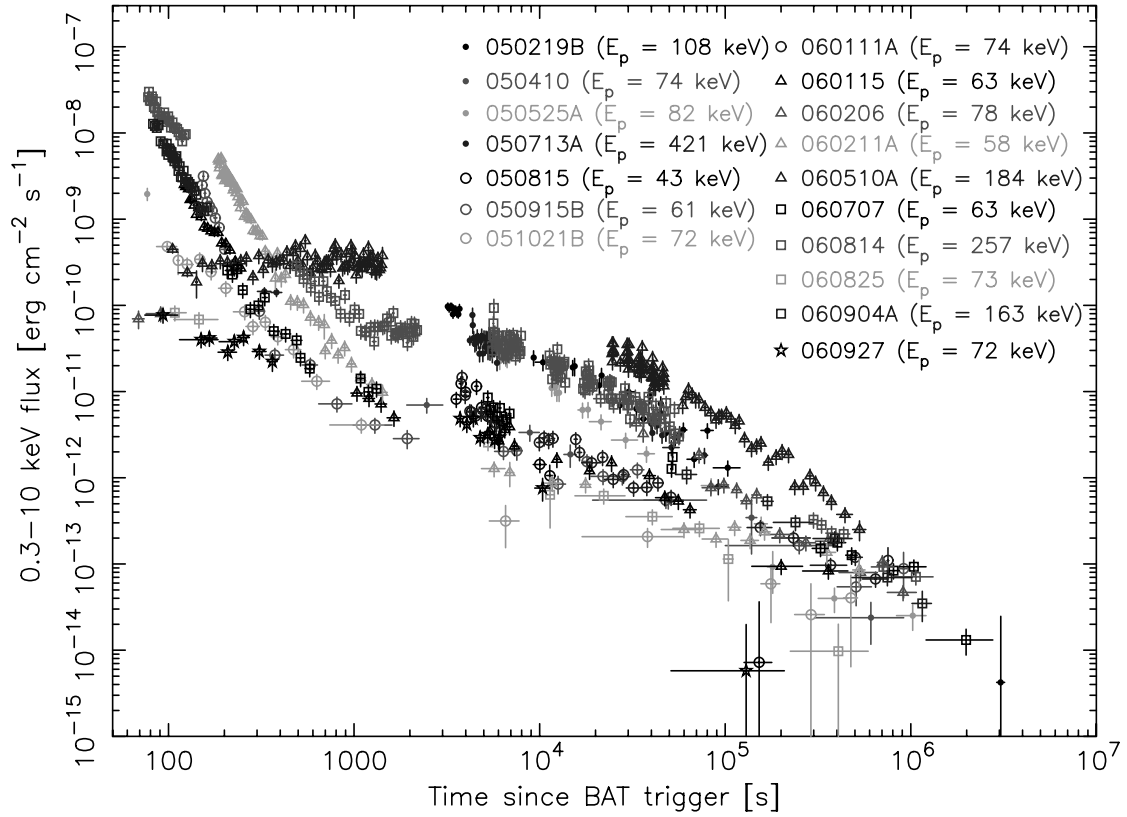


Fig. 12.—Composite plot of the 0.3–10 keV X-ray afterglow light curves of XRRs. [See the electronic edition of the Journal for a color version of this figure.]

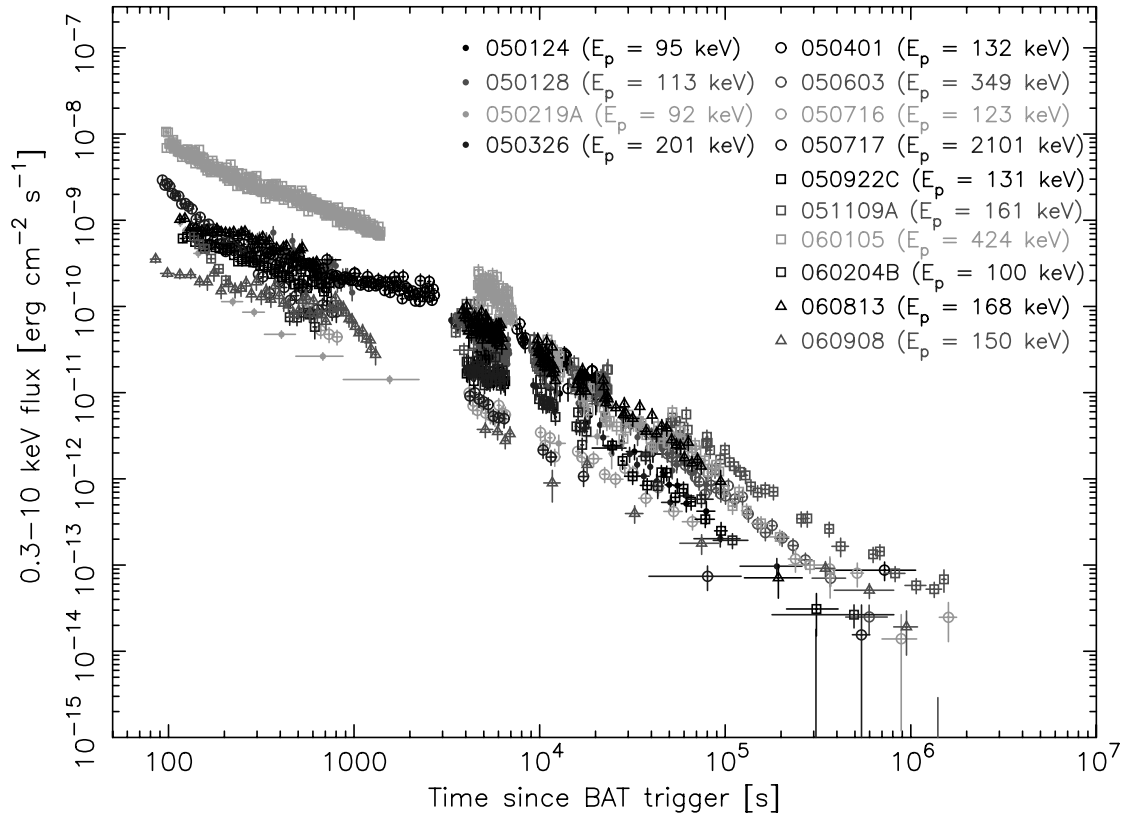


Fig. 13.—Composite plot of the 0.3–10 keV X-ray afterglow light curves of C-GRBs. [See the electronic edition of the Journal for a color version of this figure.]

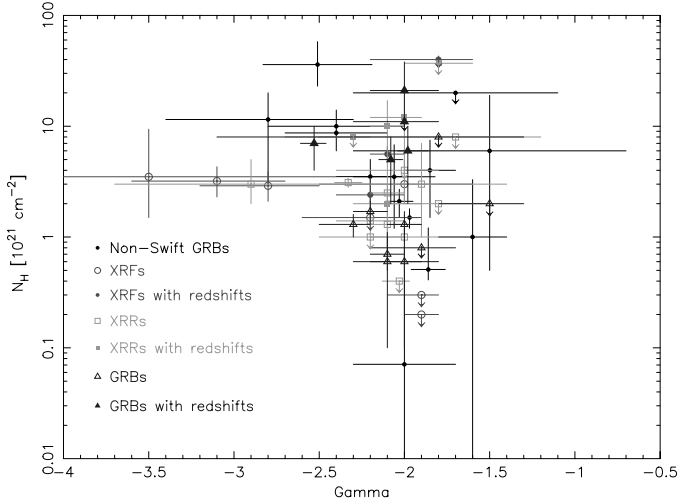


FIG. 14.—Plot of the best-fit neutral hydrogen column densities N_{H} and photon indices Γ of X-ray afterglows in our sample, along with values taken from Frontera (2003). The values plotted here of the *Swift* sample are taken from the PC mode spectra. *Swift* XRFs, XRRs, C-GRBs and non-*Swift* samples are shown as circles, squares, triangles and dots, respectively. [See the electronic edition of the *Journal* for a color version of this figure.]

in that they are concentrated around -1 and only one sample is steeper than -1.5 . On the other hand, $\alpha_{1 \text{ day}}$ of XRRs and C-GRBs are much more widely spread. Moreover, there might be a hint that XRRs and C-GRBs have a systematically steeper $\alpha_{1 \text{ day}}$ than XRFs. The correlation coefficient between $\alpha_{1 \text{ day}}$ and $E_{\text{peak}}^{\text{obs}}$ has been calculated using the same method for which we apply to calculate the correlation coefficient between $E_{\text{peak}}^{\text{obs}}$ and the fluence in the 1–1000 keV band (§ 3). We investigate the correlation coefficient for (1) GRBs without XRFs and GRB 050717, which is an outlier with $E_{\text{peak}}^{\text{obs}}$ of 2 MeV (sample A; total 26 GRBs); (2) GRBs without GRB 050717 (sample B; total 35 GRBs); and (3) all 36 GRBs (sample C) to evaluate the systematic effect due to significantly low or high $E_{\text{peak}}^{\text{obs}}$ values compared with the rest of the samples. We find the correlation coefficients of $-0.44^{+0.07}_{-0.08}$, $-0.44^{+0.04}_{-0.07}$, and $-0.49^{+0.04}_{-0.06}$ (all 1σ errors) for samples A, B, and C, respectively. The probabilities of a chance occurrence in each sample size are 7.1×10^{-3} – 6.7×10^{-2} , $2.0 \times$

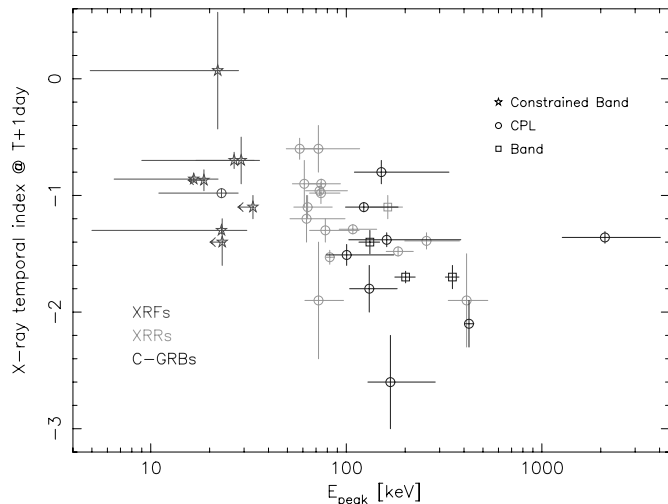


FIG. 15.—Plot of the temporal decay indices measured 1 day after the burst and $E_{\text{peak}}^{\text{obs}}$ of XRFs, XRRs, and C-GRBs. $E_{\text{peak}}^{\text{obs}}$ values derived from a *constrained* Band function, a CPL, and the Band function are marked as stars, circles, and squares, respectively. [See the electronic edition of the *Journal* for a color version of this figure.]

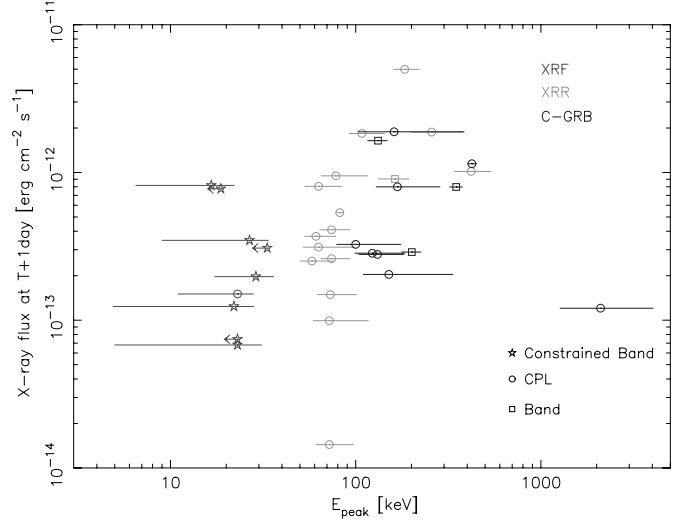


FIG. 16.—Plot of the X-ray unabsorbed flux measured 1 day after the burst and $E_{\text{peak}}^{\text{obs}}$ of XRFs, XRRs, and C-GRBs. $E_{\text{peak}}^{\text{obs}}$ values derived from a *constrained* Band function, a CPL, and the Band function are marked as stars, circles, and squares, respectively. [See the electronic edition of the *Journal* for a color version of this figure.]

10^{-3} – 1.9×10^{-2} , and 5.9×10^{-4} – 6.3×10^{-3} in the 1σ interval for samples A, B, and C, respectively. Therefore, if we include the XRF sample, the correlation between $\alpha_{1 \text{ day}}$ and $E_{\text{peak}}^{\text{obs}}$ is significant at the $>99.98\%$ level.

The relationship between the unabsorbed X-ray afterglow flux at 1 day after the burst and $E_{\text{peak}}^{\text{obs}}$ is shown in Figure 16. We calculate the correlation coefficient between the X-ray flux and $E_{\text{peak}}^{\text{obs}}$ by the same method and also for the same three samples as we used in the correlation study between $\alpha_{1 \text{ day}}$ and $E_{\text{peak}}^{\text{obs}}$ (Fig. 15). The calculated correlation coefficients are $+0.48^{+0.03}_{-0.07}$, $+0.44^{+0.05}_{-0.04}$, and $+0.31^{+0.04}_{-0.04}$ (all 1σ errors) for samples A, B, and C, respectively. The chance probabilities are 3.5×10^{-2} – 8.5×10^{-3} , 1.9×10^{-2} – 3.2×10^{-3} , and 1.2×10^{-1} – 3.9×10^{-2} in 1σ intervals for samples A, B, and C, respectively. Therefore, there is no significant correlation between the X-ray flux and $E_{\text{peak}}^{\text{obs}}$ if we investigate for all 36 bursts (sample C). However, the correlation becomes significant if we exclude GRB 050717, which is an outlier with $E_{\text{peak}}^{\text{obs}}$ of 2 MeV. Therefore, there might be a hint of a correlation between the X-ray flux at 1 day after the burst and $E_{\text{peak}}^{\text{obs}}$.

Figure 17 shows the composite X-ray luminosity light curves for the known redshift GRBs in our sample. The k -correction²⁰ has been applied to derive the 0.3–10 keV luminosities from the X-ray fluxes of each light curve bin using the best-fit PL photon index of the WT and the PC mode spectra. The time dilation effect of the cosmic expansion is taken into account in these light curves. The colors in the light curves are coded in the following ways: $E_{\text{peak}}^{\text{src}} < 100$ keV in dark gray (hereafter, XRF_{src}, as XRF in the GRB rest frame), $100 \text{ keV} < E_{\text{peak}}^{\text{src}} < 300$ keV in light gray (hereafter, XRR_{src}, as XRR in the GRB rest frame), and $E_{\text{peak}}^{\text{src}} > 300$ keV in black (hereafter, C-GRB_{src}, as C-GRB in the GRB rest frame). As illustrated in the figure, there are clear separations between XRF_{src}, XRR_{src}, and C-GRB_{src} in the overall luminosities of the X-ray light curves. XRF_{src} have less luminosity by a factor of 2 or more compared to XRR_{src} and C-GRB_{src}. Figures 18 and 19 show the X-ray temporal index and the luminosity, respectively, at 10 hr after the burst in the GRB rest frame as a function of $E_{\text{peak}}^{\text{src}}$. As seen in the observer’s frame (Figs. 15 and 16), there are weak correlations between

²⁰ The 0.3–10 keV luminosity, $L_{0.3-10}$, is calculated by $L_{0.3-10} = 4\pi d_L^2 (1+z)^{-\Gamma-2} F_{0.3-10}$, where d_L is the luminosity distance, Γ is the photon index of the XRT spectra (Table 3), and $F_{0.3-10}$ is the observed flux in the 0.3–10 keV band.

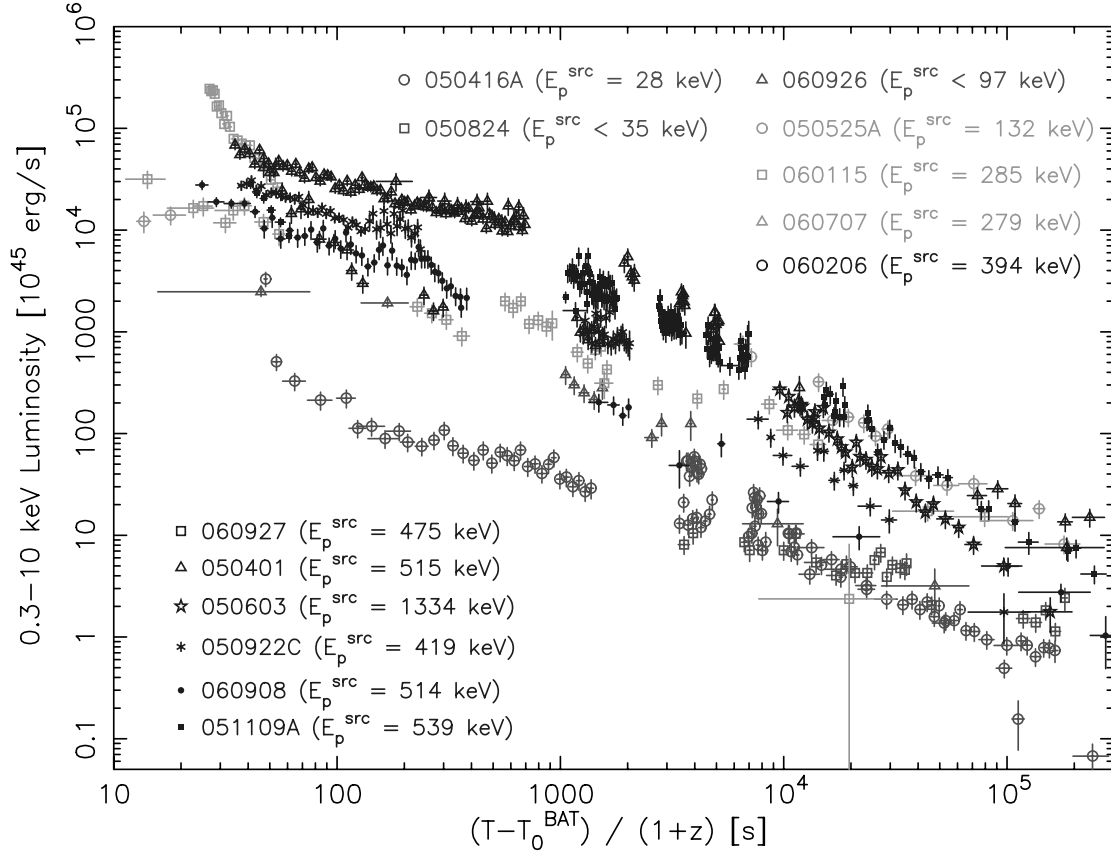


FIG. 17.— Composite X-ray luminosity afterglow light curves for known redshift GRBs in our sample. GRBs with $E_{\text{peak}}^{\text{src}} < 100$ keV, $100 \text{ keV} < E_{\text{peak}}^{\text{src}} < 300$ keV, and $E_{\text{peak}}^{\text{src}} > 300$ keV are shown. T_0^{BAT} refers to the BAT trigger time. [See the electronic edition of the Journal for a color version of this figure.]

$E_{\text{peak}}^{\text{src}}$ and the temporal index and the luminosity. The correlation coefficients between $E_{\text{peak}}^{\text{src}}$ and the temporal index, and between $E_{\text{peak}}^{\text{src}}$ and the luminosity at 10 hr, are -0.53 and $+0.72$ in both samples of 12.²¹ The chance probabilities are 0.075 and 0.008. The global trend in the X-ray luminosity light curve is that XRFs_{src} have a temporal index of $\alpha \sim -1$ and smaller

²¹ We exclude GRB 060927 because there is no X-ray data around 10 hr at the GRB rest frame.

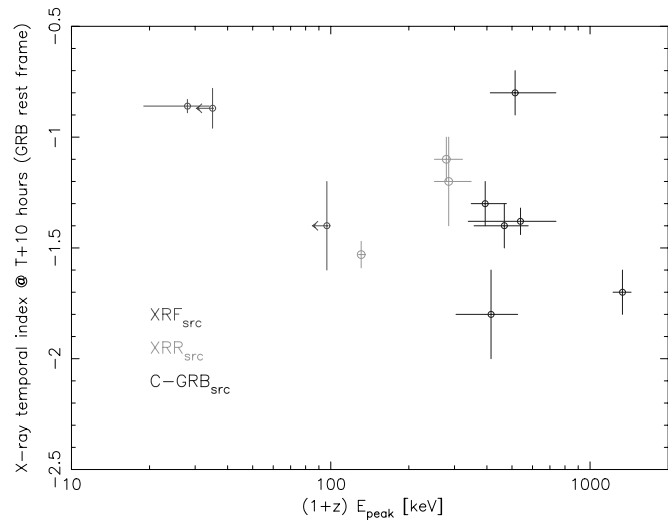


FIG. 18.— Plot of the X-ray temporal index measured at 10 hr after the burst in the GRB rest frame and $E_{\text{peak}}^{\text{src}}$. [See the electronic edition of the Journal for a color version of this figure.]

luminosities at 10 hr after the burst compared to those of XRRs_{src} and C-GRBs_{src}.

5. DISCUSSION

5.1. Characteristics between the Prompt Emission and the X-Ray Afterglow

The results of our analysis strengthen the case that XRFs and long-duration C-GRBs are not separate and distinct phenomena,

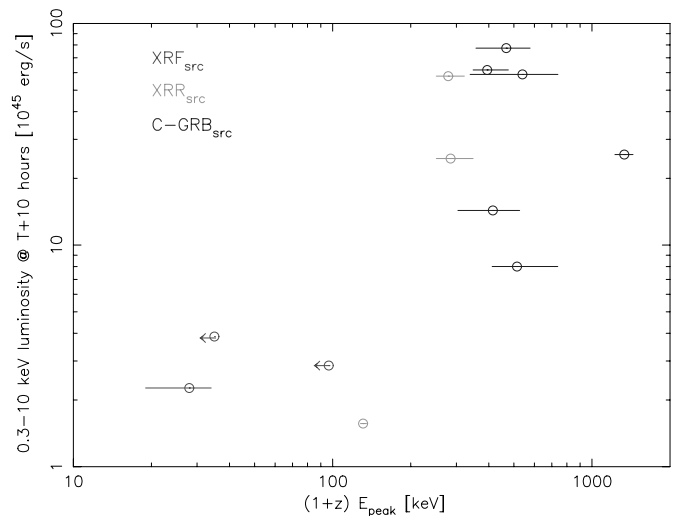


FIG. 19.— Plot of the 0.3–10 keV luminosity measured at 10 hr after the burst in the GRB rest frame and $E_{\text{peak}}^{\text{src}}$. [See the electronic edition of the Journal for a color version of this figure.]

but instead are simply ranges along a single continuum describing some sort of broader phenomenon. As Figure 4 illustrates, XRFs, XRRs, and C-GRBs form a continuum in peak energies $E_{\text{peak}}^{\text{obs}}$, with XRF $E_{\text{peak}}^{\text{obs}}$ values tending to be lower than those of XRRs, which in turn are lower than those of C-GRBs. Further evidence of the continuous nature of these phenomena comes from the continuity in the fluences of XRFs, XRRs, and C-GRBs, with XRFs tending to manifest lower fluences than XRRs, which tend to have lower fluences than C-GRBs. This is illustrated by the correlation between fluences and $E_{\text{peak}}^{\text{obs}}$ shown in Figure 6. We also confirmed the existence of the extension of the $E_{\text{peak}}^{\text{src}}-E_{\text{iso}}$ relation (Amati et al. 2002) to XRFs using our limited sample of known redshift GRBs.

As we examine the X-ray afterglow properties of XRFs, XRRs, and C-GRBs, we note that their spectral indices and natural hydrogen column densities show no strong correlation to indicate that the spectra of XRF afterglows are distinctly different from those of XRRs or C-GRBs. We do, however, note a possible distinction in the shape of the afterglow light curves among XRFs, XRRs, and C-GRBs.

We find that the C-GRBs in our sample tend to have afterglows with shallow decay indices ($-1.3 < \alpha < -0.2$) at early times followed by steeper indices ($-2.0 < \alpha < -1.2$) at later times and that the breaks between these two indices occur at about 10^3-10^4 s. XRF afterglows, on the other hand, seem to follow a different pattern. They often show a fairly shallow decay index ($-1.2 < \alpha < 0$) until the end of the XRT observation without any significant break to $\alpha < -1.2$. The afterglows of the XRRs in our sample were split between these two behaviors, with some manifesting a pattern like the XRF sample and others a pattern like the C-GRB sample (Figs. 10–13). It is possible that these two patterns form a continuum, with the break between shallow index and steep index occurring at later times for XRFs (sometimes after the afterglow has faded below our detection threshold) and at earlier times for C-GRBs (Fig. 15). There is, however, another possibility that this shallow-to-steep decay only exists in high E_{peak} GRBs. Furthermore, using our limited known redshift GRB sample, we confirmed our findings of the global features of the X-ray afterglows in the X-ray light curves in the GRB rest frame (Figs. 18 and 19). Thus, the transition from a shallow to steep decay around 10^3-10^4 s commonly seen in XRT light curves might somehow be related to the E_{peak} of its prompt emission (Fig. 20). Note that, however, two C-GRBs, GRB 050716 and GRB 060908, show a relatively shallow decay index without breaks up to 10^6-10^7 s after the trigger and thus have the same afterglow behaviors as XRFs.

5.2. Difference in the X-Ray Afterglow Luminosities

As noted by Gendre et al. (2007) we also found differences in the luminosity of the X-ray light curves measured in the GRB rest frame. The luminosity of the global X-ray light curve is brighter when $E_{\text{peak}}^{\text{src}}$ is higher (Fig. 17). According to Liang & Zhang (2006) there are two categories in the luminosity evolution of the optical afterglow. They found that the dim group (having optical luminosities at 1 day of $\sim 5.3 \times 10^{44}$ ergs s^{-1}) all appear at redshifts lower than 1.1. Motivated by their finding, we investigated $E_{\text{peak}}^{\text{src}}$ of the Liang & Zhang (2006) sample using the values quoted in Amati (2006). We noticed that the $E_{\text{peak}}^{\text{src}}$ values from their dim group are < 200 keV. The average $E_{\text{peak}}^{\text{src}}$ of their dim group is 96 keV, which would be XRFs_{src} in our classification. On the other hand, the average $E_{\text{peak}}^{\text{src}}$ values from the bright group in their sample is 543 keV. Therefore, the trend that we found in the overall luminosity of the X-ray light curves might be consistent with the optical light curves. However, the

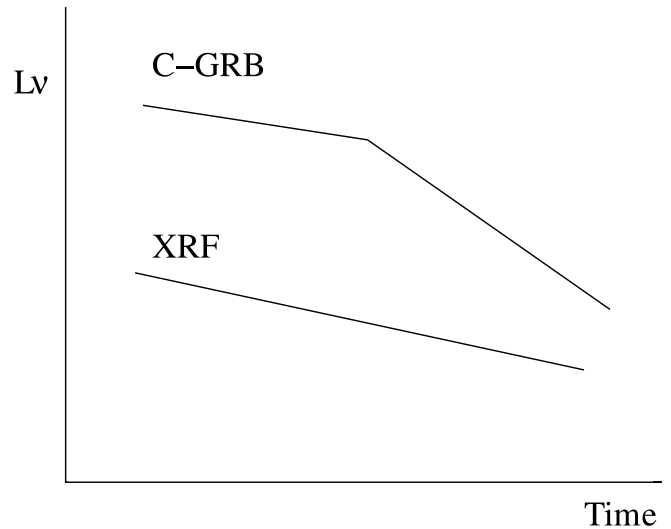


FIG. 20.— Schematic figure of XRF and C-GRB X-ray afterglow light curves. C-GRB afterglows tend to have a shallow index followed by a steeper index, with a break around 10^3-10^4 s after the burst. XRF afterglows, on the other hand, tend to have a shallow index without a break of significant change in the decay index. Furthermore, the overall luminosity of XRF afterglows is factor of 2 or more less luminous than that of C-GRBs.

break from a shallow-to-steep decay in the X-ray light curve that we see preferentially in C-GRBs is not usually observed in the optical band (e.g., Panaitescu et al. 2006). These similar and distinct characteristics in the X-ray and the optical afterglow light curves, together with the correlation in $E_{\text{peak}}^{\text{src}}$, are important characteristics in seeking to understand the nature of the shallow-to-steep decay component in the X-ray afterglow data.

5.3. Understanding the Shallow-to-Steep Decay by Geometrical Jet Models

There are several theoretical models that explain a shallow-to-steep decay break. They are (1) the energy injection from the central engine or late time internal shocks (e.g., Nousek et al. 2006; Zhang et al. 2006; Ghisellini et al. 2007; Panaitescu 2007); (2) the geometrical jet models (e.g., Eichler & Granot 2006; Toma et al. 2006); (3) the reverse shock (Genet et al. 2007; Uhm & Beloborodov 2007); (4) time-varying microphysical parameters of the afterglow (Ioka et al. 2006); or (5) the dust scattering of prompt X-ray emission (Shao & Dai 2007). Here we focus on the geometrical jet models, which have a tight connection between the prompt and afterglow emission properties. Eichler & Granot (2006) investigated a thick ring jet (cross section of a jet in the shape of a ring) observed at slightly off-axis from the jet. They can reproduce the shallow-to-steep decay feature in the X-ray afterglow with their thick ring jet model with the appearance of an off-axis afterglow emission at late times. Because of the relativistic beaming effect in this model, the observer, who is observing the ring jet from an off-axis direction, should see a softer prompt emission. Therefore, we would expect to see a shallow-to-steep decay in the X-ray light curve more frequently for XRFs and rarely for C-GRBs. Our findings contradict this prediction of the model. Another jet model that can produce a shallow-to-steep decay light curve is an inhomogeneous jet model (Toma et al. 2006). A shallow-to-steep decay phase of the light curve may be produced by the superposition of the subject emissions, which are launched slightly off-axis from the observer. The prediction of this jet model is that a shallow-to-steep decay should coexist with high $E_{\text{peak}}^{\text{src}}$ in GRBs (an observer has to

observe the prompt subject emission from on-axis), and XRFs will have a conventional afterglow light curve. Our results agree quite nicely with this prediction. However, considering the non-existence of a shallow-to-steep phase in the optical light curve, it is hard to understand why this shallow-to-steep phase only exists in the X-ray band in the framework of these jet models. Further simultaneous X-ray and optical afterglow observations along with a detailed modeling of afterglows taking into account the prompt emission properties such as E_{peak} will be needed to solve the origin of this mysterious shallow-to-steep decay feature.

6. CONCLUSION

We have seen that the XRFs observed by *Swift* form a continuum with the C-GRBs observed by *Swift* and by other missions, having systematically lower fluences and lower $E_{\text{peak}}^{\text{obs}}$ than C-GRBs.

We have noted that the X-ray light curves of XRFs tend to follow a different “template” than those of C-GRBs. The light curves of the C-GRB afterglows show a break to steeper indices (shallow-to-steep decay) at earlier times, whereas XRF afterglows show no such break. This break is evident in the X-ray but not in the optical light curve. Moreover, the overall luminosity of XRF X-ray afterglows is smaller by a factor of 2 or more compared to that of C-GRBs. These distinct differences in the X-ray afterglow between XRFs and C-GRBs are keys to understanding

not only the shallow-to-steep decay phase in the X-ray afterglow but also the nature of XRFs in a unified picture.

We have discussed the geometrical jet models based on the trend we found that the shallow-to-steep break in the X-ray afterglow preferentially is seen in the C-GRB sample. We concluded that none of the jet models can explain the behavior of a shallow-to-steep decay phase observed only in the X-ray afterglow. We also emphasize the importance of having simultaneous X-ray and optical afterglow observations along with the characteristics of prompt emission such as $E_{\text{peak}}^{\text{obs}}$ to constrain the various geometrical jet models.

We would like to thank the anonymous referee for comments and suggestions that materially improved the paper. This research was performed while T. S. participated in a NASA Postdoctoral Program administered by Oak Ridge Associated Universities at NASA Goddard Space Flight Center. R. Y. was supported in part by Grants-in-Aid for Scientific Research of the Japanese Ministry of Education, Culture, Sports, Science, and Technology 18740153. The material of the paper has been improved by the discussions during the workshop “Implications of *Swift*’s Discoveries about Gamma-Ray Bursts” at the Aspen Center for Physics.

REFERENCES

- Amati, L. 2006, *MNRAS*, 372, 233
 Amati, L., et al. 2002, *A&A*, 390, 81
 Barthelmy, S. D., et al. 2005, *Space Sci. Rev.*, 120, 143
 Band, D. L. 2003, *ApJ*, 588, 945
 ———. 2006, *ApJ*, 644, 378
 Band, D. L., et al. 1993, *ApJ*, 413, 281
 Barraud, C., Daigne, F., Mochkovitch, R., & Atteia, J. L. 2005, *A&A*, 440, 809
 Barraud, C., et al. 2003, *A&A*, 440, 809
 Burrows, S. D., et al. 2005a, *Space Sci. Rev.*, 120, 165
 ———. 2005b, *Science*, 309, 1833B
 Cabrera, J. I., Firmani, C., Avila-Reese, V., Ghirlanda, G., Ghisellini, G., & Nava, L. 2007, *MNRAS*, 382, 342
 Campana, S., et al. 2006, *A&A*, 449, 61
 Chincarini, G., et al. 2007, *ApJ*, 671, 1903
 Crew, G., et al. 2005, *GCN Circ.* 4021, <http://gcn.gsfc.nasa.gov/gcn3/4021.gcn3>
 D’Alessio, V., Piro, L., & Rossi, E. M. 2006, *A&A*, 460, 653
 Dermer, C. D., Chiang, J., & Böttcher, M. 1999, *ApJ*, 513, 656
 Dermer, C. D., & Mitman, K. E. 2003, in *ASP Conf. Ser. 312, Third Rome Workshop on Gamma-Ray Bursts in the Afterglow Era*, ed. M. Feroci et al. (San Francisco: ASP), 301
 Dickey, J. M., & Lockman, F. J. 1990, *ARA&A*, 28, 215
 Evans, P. A., et al. 2007, *A&A*, 469, 379
 Eichler, D., & Granot, J. 2006, *ApJ*, 641, L5
 Frontera, F. 2003, in *Lecture Notes in Phys. 598, Supernovae and Gamma Ray Bursters*, ed. K. Weiler (New York: Springer), 317
 ———. 2004, in *ASP Conf. Ser. 312, Proc. Third Rome Workshop: Gamma-Ray Bursts*, ed. M. Feroci et al. (San Francisco: ASP), 3
 Gehrels, N., et al. 2004, *ApJ*, 611, 1005
 Gendre, B., Galli, A., & Piro, L. 2007, *A&A*, 465, L13
 Genet, F., Daigne, F., & Mochkovitch, R. 2007, *MNRAS*, 381, 732
 Ghisellini, G., Ghirlanda, G., Nava, L., & Firmani, C. 2007, *ApJ*, 658, 75
 Golenetskii, S., et al. 2005a, *GCN Circ.* 3152, <http://gcn.gsfc.nasa.gov/gcn3/3152.gcn3>
 ———. 2005b, *GCN Circ.* 3179, <http://gcn.gsfc.nasa.gov/gcn3/3179.gcn3>
 ———. 2005c, *GCN Circ.* 3518, <http://gcn.gsfc.nasa.gov/gcn3/3518.gcn3>
 ———. 2005d, *GCN Circ.* 4238, <http://gcn.gsfc.nasa.gov/gcn3/4238.gcn3>
 ———. 2006a, *GCN Circ.* 5113, <http://gcn.gsfc.nasa.gov/gcn3/5113.gcn3>
 ———. 2006b, *GCN Circ.* 5264, <http://gcn.gsfc.nasa.gov/gcn3/5264.gcn3>
 ———. 2006c, *GCN Circ.* 5460, <http://gcn.gsfc.nasa.gov/gcn3/5460.gcn3>
 ———. 2006d, *GCN Circ.* 5518, <http://gcn.gsfc.nasa.gov/gcn3/5518.gcn3>
 Gotthelf, E. V., Hamilton, T. T., & Helfand, D. J. 1996, *ApJ*, 466, 779
 Grupe, D., et al. 2007, *AJ*, 133, 2216
 Heise, J., in ‘t Zand, J. J. M., Kippen, R. M., & Woods, P. M. 2003, in *Proc. Second Rome Workshop: Gamma-Ray Bursts in the Afterglow Era*, ed. E. Costa, F. Frontera, & J. Hjorth (Berlin: Springer), 16
 Ioka, K., Toma, K., Yamazaki, R., & Nakamura, T. 2006, *A&A*, 458, 7
 Kaneko, Y., et al. 2006, *ApJS*, 166, 298
 Kippen, R. M., Woods, P. M., Heise, J., in ‘t Zand, J. J. M., Briggs, M. S., & Preece, R. D. 2003, in *AIP Conf. Proc. 662, Gamma-Ray Burst and Afterglow Astronomy 2001*, ed. G. R. Ricker & R. K. Vanderspek (New York: AIP), 244
 Kocevski, D., Butler, N., & Bloom, J. S. 2007, *ApJ*, 667, 1024
 Krimm, H. A., et al. 2006, *ApJ*, 648, 1117
 Lamb, D. Q., Donaghy, T. Q., Graziani, C. 2005, *ApJ*, 620, 355
 Liang, E. W., & Zhang, B. 2006a, *ApJ*, 638, L67
 Liang, E. W., et al. 2006b, *ApJ*, 646, 351
 Mészáros, P., Ramirez-Ruiz, E., Rees, M. J., & Zhang, B. 2002, *ApJ*, 578, 812
 Mochkovitch, R., Daigne, F., Barraud, C., & Atteia, J. L. 2003, in *ASP Conf. Ser. 312, Third Rome Workshop on Gamma-Ray Bursts in the Afterglow Era*, ed. M. Feroci et al. (San Francisco: ASP), 381
 Morris, D. C., et al. 2007, *ApJ*, 654, 413
 Nousek, J. A., et al. 2006, *ApJ*, 642, 389
 O’Brien, P., et al. 2006, *ApJ*, 647, 1213
 Paciesas, W. S., et al. 1999, *ApJS*, 122, 465
 Panaitescu, A. 2007, *MNRAS*, 379, 331
 Panaitescu, A., et al. 2006, *MNRAS*, 369, 2059
 Preece, R. D., et al. 2000, *ApJS*, 126, 19
 Romano, P., et al. 2006, *A&A*, 456, 917
 Rossi, E., Lazzati, D., & Rees, M. J. 2002, *MNRAS*, 332, 945
 Sakamoto, T., et al. 2004, *ApJ*, 602, 875
 ———. 2005, *ApJ*, 629, 311
 ———. 2006, *ApJ*, 636, 73
 ———. 2007, *ApJ*, 669, 1115
 ———. 2008, *ApJS*, in press
 Shao, L., & Dai, Z. 2007, *ApJ*, 660, 1319
 Shirasaki, Y., et al. 2003, *PASJ*, 55, 1033
 Strohmayer, T. E., Fenimore, E. E., Murakami, T., & Yoshida, A. 1998, *ApJ*, 500, 873
 Tashiro, M. S., et al. 2007, *PASJ*, 59, 361
 Toma, K., Ioka, K., Yamazaki, R., & Nakamura, T. 2006, *ApJ*, 640, L139
 Toma, K., Yamazaki, R., & Nakamura, T. 2005, *ApJ*, 635, 481
 Uhm, Z. L., & Beloborodov, A. M. 2007, *ApJ*, 665, 93
 Ulanov, M. V., et al. 2005, *Nuovo Cimento C*, 28, 351
 Willingale, R., et al. 2007, *ApJ*, 662, 1093
 Woosley, S. E., Zhang, W., & Heger, A. 2003, in *AIP Conf. Proc. 662, Gamma-Ray Bursts and Afterglow Astronomy 2001*, ed. G. R. Ricker & R. Vanderspek (New York: AIP), 185
 Yamazaki, R., Ioka, K., & Nakamura, T. 2002, *ApJ*, 571, L31
 ———. 2004, *ApJ*, 607, L103
 Zhang, B., Dai, X., Lloyd-Ronning, N., & Meszaros, P. 2004, *ApJ*, 601, 119
 Zhang, B., Mészáros, P. 2002, *ApJ*, 571, 876
 Zhang, B., et al. 2006, *ApJ*, 642, 354